10-2018

Study of the Femtosecond Laser Processed Surfaces, Imprinting, and Casting for Changing the Wettability of Surfaces

Yingxiao Song
University of Nebraska - Lincoln, yingxiaosong1@gmail.com

STUDY OF THE FEMTOSECOND LASER PROCESSED SURFACES, IMPRINTING, AND CASTING FOR CHANGING THE WETTABILITY OF SURFACES

by

Yingxiao Song

A DISSERTATION

Presented to the Faculty of

The Graduate College at the University of Nebraska

In Partial Fulfillment of Requirements

For the Degree of Doctor of Philosophy

Major: Materials Engineering

Under the Supervision of Professor Jeffrey Shield

Lincoln, Nebraska

October, 2018

DISSERTATION TITLE

STUDY OF THE FEMTOSECOND LASER PROCESSED SURFACES, IMPRINTING, AND CASTING FOR CHANGING THE WETTABILITY OF SURFACES

BY

Yingxiao Song

SUPERVISORY COMMITTEE:

DISSERTATION CHAIR SIGNATURE	DATE	10/26/18
COMMITTEE MEMBER SIGNATURE	DATE	10/26/2018
COMMITTEE MEMBER SIGNATURE	DATE	10/26/2018
COMMITTEE MEMBER SIGNATURE	DATE	10/26/2018

UNIVERSITY OF Nebraska Lincoln

STUDY OF THE FEMTOSECOND LASER PROCESSED SURFACES, IMPRINTING, AND CASTING FOR CHANGING THE WETTABILITY OF SURFACES

Yingxiao Song, Ph.D.

University of Nebraska, 2018

Adviser: Jeffrey Shield

Femtosecond Laser Surface Processing (FLSP) is a technology to fabricate micro/nano surface structures. These patterned surface structures show great importance in many applications, especially in controlling the wettability of the surface. Imprinting is a typical method for manufacturing large volumes of surfaces. This study combines two processes (FLSP and stamping) together to produce a surface structure similar to the original FLSP surface. In the first step, micro/nano structured surface mounds were fabricated by femtosecond laser processing. Then, these FLSP surfaces served as molds for subsequent imprinting to replicated the "negative" surface on a blank material. Surface morphology and peak-to-valley roughness of the imprinted surface was used to quantify the imprint quality, while droplets tests were conducted to measure the wetting property of the surface.

The imprinting experiments had two parallel branches, one was stamping, the other was casting. Stamping experiments were conducted on different materials. These materials were divided into metals and polymers. A finite element model for single mound stamping was investigated to study the influence of material and geometry. The model

was verified by experiments. A variety of experiments were conducted to investigate the effect of temperature and pressure on the imprint quality. Different FLSP surface stamps were also produced to investigate the morphology's influence on the imprinted surface as well. Casting experiments were conducted twice to produce "negative" and "positive" surfaces related with the FLSP surface. These imprinted surfaces had changed their wetting property due to the patterned surface structure.

An anti-icing test was conducted on these imprinted sample surfaces. The results from this test showed that the anti-icing property of material was related to its wetting behavior. The superhydrophobic surface had the best performance for anti-icing.

Acknowledgements

I am immensely grateful to my adviser, Dr. Jeffrey Shield, for his support and guidance over the years. Without his trust and support, I never would have the opportunity to go on my studies at the University Nebraska-Lincoln and conduct the research presented in this dissertation.

I would also like to express my gratitude to Dr. Dennis Alexander, Dr. Jian Wang and Dr. Bai Cui for serving as my supervisory committee members and providing valuable feedback.

I am also grateful to our collaborators from the Electrical and Computer Engineering Departments-Dr. Dennis Alexander, Dr. Craig Zuhlke and all the students from the Center for Electro-Optics and Functionalized Surface (CEFS). Special thanks to Aaron Ediger, Ryan Bell, and Alfred Tsubaki for producing FLSP samples for this research. I also thank Chongji Huang for the condensation experiment. I would also like to express my gratitude to Dr. Gogos for his suggestions on the stamping model. I also thank Dr.Ndao and his students, Anton Hassebrook, Ethan Davis and Sarah Wallis for contact angle experiments. I also want to say thanks to Wenlong Li for the compression machine selection and Dr. Ehsan Rezaei for the nanoindentation experiments.

I would also like to thank all the members in my laboratory for their help and friendship, particularly Dr. Edwin Peng, Dr. Meiyu Wang, and Dr. Mak Koten for their help in SEM and FIB, and Zahra Ahmadi for her help in nanoparticle deposition. I also thank

Soodabeh Azadehranjbar, James Doyle, Mark Anderson for their support at group meeting. I also thank all the staff in the Department of Mechanical and Materials Engineering, Heidi, Kathie Hiatt, Cherie Crist, and Mary Ramsier for their assistance throughout my graduate career. I also thank all the friends I made here in Lincoln, since they made my life in Lincoln exciting and enjoyable.

Last but not the least, I would like to thank my mother for her encouragement and support of my education for the past 24 years. She always inspires me by her behavior. Without her, I would not take actions to be the one I want to be. Another special thanks to my cats: Meow Meow and Bin Bin, who bring me happiness when I am depressed.

Contents

List of Figures

Chapter 1. Introduction

Surface morphology is one of the most important surface characteristics for controlling the wettability of a surface. An imprint of a femtosecond laser processed surface is used to duplicate the self-organized surface morphology from the femtosecond laser processed surface to another material surfaces. This chapter gives the explanation of the surface morphology's importance, and its close connection with many material properties, especially wetting properties. At the end of this chapter, the thesis structure will be overviewed.

1.1 Surface morphology VS. materials properties

The surface of a solid is constructed by free bounding faces forming interfaces with the environment. These free bounding faces are known as a surface phase. Morphology is one of the most significant material surface characteristics, which affects many material properties. Morphological features of the surface in both micro and nanoscale levels are important factors determining the wear and corrosion behavior of the materials. A large variety of studies have shown that surface morphology directly leads to different material properties from various aspects like mechanical strength, dynamic property, optical visibility, heat transfer efficiency, wettability etc. [1]–[7].

Surface morphology, or surface roughness, influences a materials mechanical strength especially at the strength-weak regions, for example joints or fragile film materials[6], [7]. Jiang et al. have conducted shear experiments related to rock joints under constant normal load and normal stiffness, proving the relationship between surface morphology and shear hydro-mechanical behavior.[7] For other fragile materials, Lohbauer et al. used to study the polymer and ceramic materials sensitivity of surface roughness on fracture strength. After excluding the effect of crystallite and polymer resin composite size, the experiments results showed that the fracture strength decreased with the increase of the surface roughness[6]. The phenomena is consistent with the nanoindentation results of bone, especially under low load experiments[5]. Regarding dynamic properties, surface roughness has been considered one of the most important factors that influence turbine performance[1], [2], [4]. For engine performance, surface morphology causes earlier boundary layer momentum loss[2]; For compressors or turbines, surface morphology plays different roles at different Reynolds numbers[1]. Surface morphology also plays an important role in light emitting devices, since most of them are composed by thin film and layer inhomogeneities which are introduced by large surface roughness[3].

1.2 Surface morphology Vs wetting property

Surface morphology is an important factor governing the wetting property of a material

surface and was a parameter studied in this research.

From the natural world, the lotus plant, with its outstanding non-wettability, attracted many researchers to explore its surface for potential application in the self-cleaning and anti-corrosive fields. The special superhydrophobic behavior (ability to repel water) of the lotus leaf surface is recognized as the famous “Lotus Effect”.[8] In 1997, Barthlott et al. was the first to find that the hierarchical micro/nanostructure of a lotus leaf surface plays a very important role in its superhydrophobicity.[9] Since then, research has explored many different surface processing techniques designed to alter the surface morphology to mimic the lotus leaf.

Surface processing techniques are also called surface treatment. Since the surface is usually the most important part of any engineering component, “surface treatment” was coined about thirty years ago. There are many surface processing techniques applied in current industry fields. The typical surface process includes coating, mechanical surface treatment and laser surface treatment.

Metals, polymer and ceramics are three major types of materials. Their compositions and properties are different from each other. So, different surface processes have different effects on these materials. This study focus on the first two materials, so this thesis emphasizes surface processes of metals and polymers.

1.3 Specific aims

Since there are so many surface processing techniques to produce different surface morphologies for their industry applications, this study is focusing on the morphology produced by femtosecond laser sueface processing (FLSP), and the wetting properties that can be formed from FLSP and imprinting the FLSP surface on other metallic surfaces. The goal of this work is to optimize a reasonable surface processing method for engineering applications. The research work was mainly focused on can producing different surface wetting properties by imprinting a similar FLSP morphology on different material surface. Fulfillment of the goal of this work is based on the completion of the following specific aims:

(a). Investigate the imprint mechanism by developing finite element models to study the sensitivity of the imprinted morphology;

(b). Select die material with enough mechanical strength, ensuring that after several stampings, the femtosecond laser induced surface mounds maintain the basic shape to apply multiple times;

(c). Characterize the imprint quality by the peak-to-valley roughness;

(d). Characterize the imprinted surface wetting behavior by static contact angle;

(e). Investigate how the load pressure and stamping temperature influence the imprinted quality on metals and polymer materials, respectively;

(f). Conduct casting to duplicate the FLSP surface and compare the results with stamping;

(g). Investigate how condensation and freezing happens on these patterned surfaces

1.4 Overview

Chapter 2 introduces the surface characterization applied in this study.

Chapter 3 introduces Femtosecond Laser Surface Processing (FLSP) techniques. FLSP is the first step of the imprint study to produce the original micro/nano scale features on the surface. The chapter introduces the multiscale surface formation mechanisms and how different FLSP surfaces were produced.

The special micro/nano surface character's connection with the wetting property is covered in Chapter 4. In this chapter, by introducing liquid-solid-vapor models, the surface wetting property is cataloged as either hydrophilic or hydrophobic. The patterned FLSP surface shows different wetting properties than various original materials and morphology plays an important role in this difference.

In chapter 5, a series of imprint experiments by stamping are conducted. These experiments include the stamping process on different metals (oxygen-free-copper and Al) and polymer materials (PC and PMMA), and how the pressure and temperature influence the stamping process. The FLSP die surface morphology's influence is also illustrated, and a finite element model is established to complement the experimental results.

Chapter 6 introduces another method to duplicate the unique FLSP surface-casting. Unlike the stamping method producing the surface morphology from compression deformation, casting applies liquid solvent and mask on the FLSP surface to capture the

morphology as a negative. Two materials were used for the casting, PDMS and PU.

The anti-icing property of the imprinted surface is studied in chapter 7. The anti-icing property was investigated by condensation and freezing experiments. The comparison between the FLSP and imprinted surfaces is presented in this chapter. The industrially important material PC was used for these experiments.

Chapter 8 shows the statistical results of the FLSP surface and duplicated ones from different aspects.

Finally, Chapter 9 summarizes this research and proposes the research potential and future applications of this study.

Chapter 2. Surface characterization

A larger number of surface characterization experiments were conducted in this study. This chapter shows the facilities and methods applied for surface characterization. Scanning electron microscopy (SEM) and laser confocal scanning microscopy (LCSM) were used to obtain the surface morphology and surface roughness. These observation techniques and facilities are introduced below.

2.1 Preparation

Before observing sample surface, all samples used as blanks were $2\ \text{cm} \times 2\ \text{cm}$, and ultrasonic baths were used to clean all the samples. These samples were then observed by SEM and LCSM.

2.2 SEM

A scanning electron microscope is a type of electron microscope that produces images of a sample by scanning the surface with a focused beam of electrons. [10] The electrons interact with atoms in the sample, producing various signals that contain information about surface morphology; the final resolution can approach 1 nanometer [11]. The interactions between the incident electrons and the sample are shown in Figure 4.1. Most of the signals generated from these interactions can be identified by different types of electron microscopes [12].

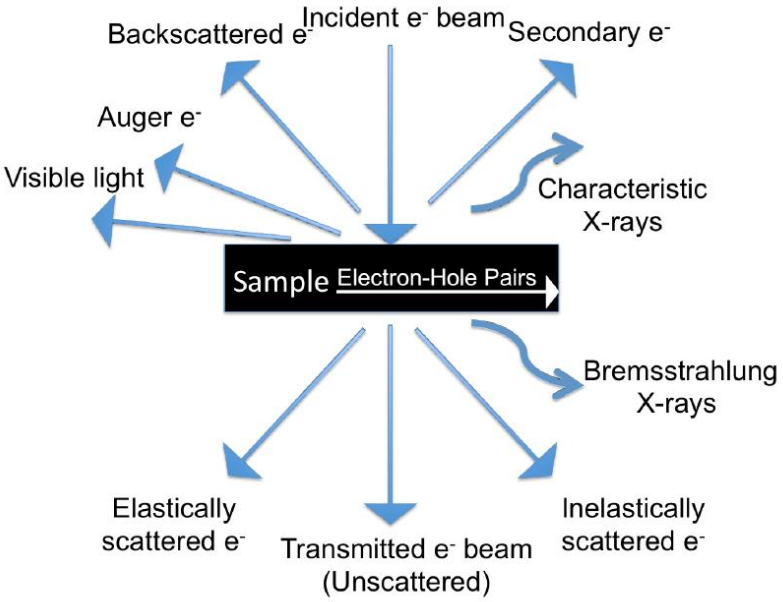

Figure 2.1 Generated signals during the interactions between the incident electrons and the samples [12], backscattered electron is important for images in this research.

As shown from Figure 2.2, the FEI Helios 660 Lab is the SEM system that was utilized in this study. This dual-beam microscope combines a monochromated field emission scanning electron microscope with a focused ion beam column for fast, precise nanomachining and nanoscale structural characterization.

Figure 2.2. FEI Helios Nano Lab 660 used in this study

2.3 Laser confocal microscope

Illustrated in Figure 2.3 is the light paths of confocal scanning microscopy. The image seen through the microscope includes the in-focus portion and the out-of-focus portion above and below the plane of focus. Confocal microscopy removes out-of-focus rays by passing the light through one or more small apertures, leaving only a thin, highly focused plane. The light from this focused plane can be digitized and stored on a computer. The distance between the specimen and the microscope objective is then changed producing a new focal plane. The new focal plane is digitized and stored. After a series of planes has been collected, individual slices can be examined or the whole specimen can be digitally reconstructed by a computer as a three-dimensional volume [13].

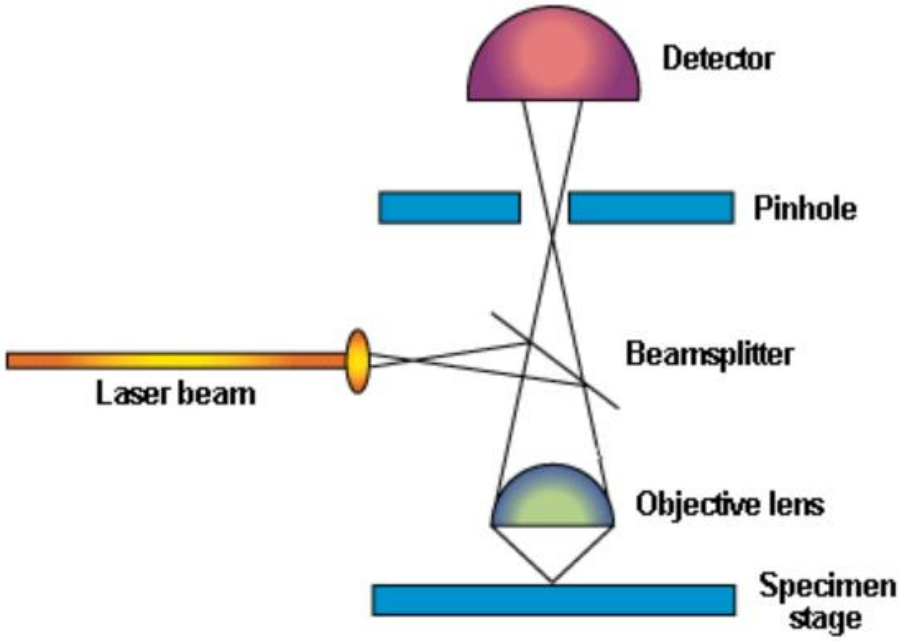

Figure 2.3 Principle of laser confocal scanning microscope

In this study, a Keyence VK-series laser scanning confocal microscope was applied to study surface morphology and roughness as shown in Figure 2.4. This instrument has the advantage of no restriction on objects, high-resolution imaging, automatic comparison and analysis of multiple surfaces and accurate measurements over a wide area.

Figure 2.4. Keyence laser scanning confocal microscope used in this study

Chapter 3. Femtosecond Laser Processed Surface (FLSP)

Femtosecond Laser Processed Surface is an outstanding technique that can produce self-organized surface structures. This chapter will introduce the development of the femtosecond laser, the mechanism of the FLSP surface formation, the application of these patterned surfaces, and various FLSP surfaces.

3.1 Review

A femtosecond laser is a laser which emits optical pulses with a duration well below one picosecond, in the domain of femtoseconds. One femtosecond equals 10^{-15} second. Lasers with this short of pulse duration falls under the category of ultrafast lasers or ultrashort pulse lasers. [14] The introduction of the femtosecond laser can trace back to 1988 [15]. Around 1994 , it use as a material nanoprocessing method was first investigated. Besides various femtosecond laser ablations, it was discovered that femtosecond laser can also produce periodic surface structures[16-21]. Since then, the femtosecond laser was used for producing a large variety of nanostructured material surfaces, because it can process nearly all types of materials, including metals, semiconductors, glasses and polymers, and even non-planar surfaces. What is more, it is a maskless single-step processing method at a high speed under normal ambient conditions, instead of a clean room environment. The femtosecond laser can also

produce nanostructures on surface areas from microscale to macroscale[17,18].

Although the femtosecond laser can produce different surface structures for a wide variety of applications, its high cost precludes the use of femtosecond lasers for large-scale manufacturing , manufactures are more apt to use non-ultrafast laser solutions if the production volumes are relatively low[22-24]. Even the cost of femtosecond laser-assisted cataract surgery is hard to afford for many families [25]. Above all, it is necessary to find an economic replacement method for obtaining similar advantages of the femtosecond laser.

3.2 Femtosecond laser and application

The femtosecond laser surface processing (hereafter, FLSP) can produce micro/nano surface structures that are similar lotus leaves, which have a good performance in hydrophobicity, self-cleaning and defense against pathogens[26]. Femtosecond lasers have many advantages: 1) formation of multiscale structure in a single step, with micro/nanoscale features controlled by laser processing parameter. 2) Structure permanency; self-organized surface structure through shaping of substrate-retain durability of substrate. 3) Contactless fabrication; open-air laser processing enables the processing of an arbitrary shaped 3D surface; 4) Scalability; large areas can be processed by scaling the laser power and repetition rate, 5) Versatility; FLSP can be extended to a wide range of materials.

3.2.1 Mechanism

The physical process of FLSP is applying laser beam focused pulse rastered over the sample surface by rastering the sample under the focused beam. Several parameters determine the finial morphology of these self-organized surface structures. These parameters are the laser fluence, the number of laser shots per area incident on the sample, and composition and pressure of the processing environment. A shot study of the structural formation as a function of the laser fluence on the self-organized surface structure was published by Zuhlke et al [27]. There are three phases for this multi-scale surface structure growth. Firstly, during subsequent laser treatment of the sample surface, a random nanostructure grows on the surface which ultimately introduces the precursor sites of the micro/nano scales of the surface. Then the precursor sites develop larger and larger self-organized characters, and at last complete the development of the final structure of the FLSP surface. This process can be observed from [27]. This is an example of a nickel sample surface mound formation by different shot numbers.

3.2.2 Application

The mound structures formed by FLSP introduces different surface properties which can be used in many fields [28]. One of the most outstanding advantages that the FLSP surface has is its special wetting behavior. The mechanism of the wetting behavior is illustrated in Chapter 4. Even immersed into the liquid, there is a transparent plastron formed by the water, which prevents water contacting with the featured surface. One

example shown here is Figure 3.1. The copper bullet was processed by FLSP followed by siloxane deposition. It is easy to distinguish the processed and unprocessed regions, as the processed regions are black. After the bullet tip is immersed into the water, a white membrane (the white color is caused by the light reflection) enclosed the black regions. It was formed by the interaction water, because the tip surface was superhydrophobic, and instead of attaching to the surface, a water membrane formed.

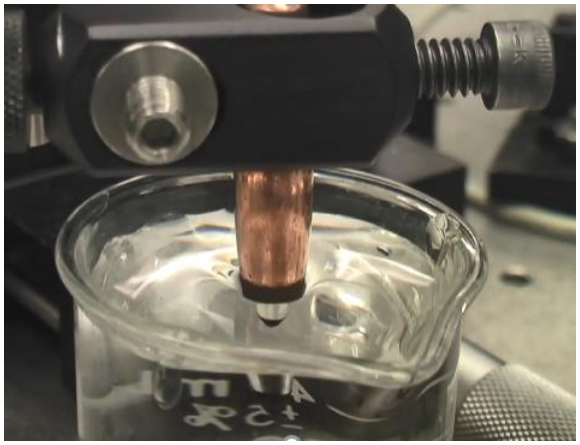

Figure 3.1 The transparent plaston(white regions due to the light reflection) indicating the FLSP region of the copper bullet (top black regions) repelling water.

FLSP can tailor the wetting behavior for specific applications. For example, Figure 3.3 shows a piece of femtosecond laser processed sample with a patterned region of superhydrophilic and superhydrophobic regions. When droplets fall on the sample surface, the different behavior of hydrophilic and superhydrophobic regions can be observed. Similarly, with the FLSP bullet tip, the superhydrophobic surface prevents water attaching to it, so a transparent plastron forms on the boundary between the surface and water droplets. For the region which is hydrophilic, the situation is opposite. The water droplets are wicked into the hydrophilic regions as soon as contacting the

surface and appear as black squares in Figure 3.2.

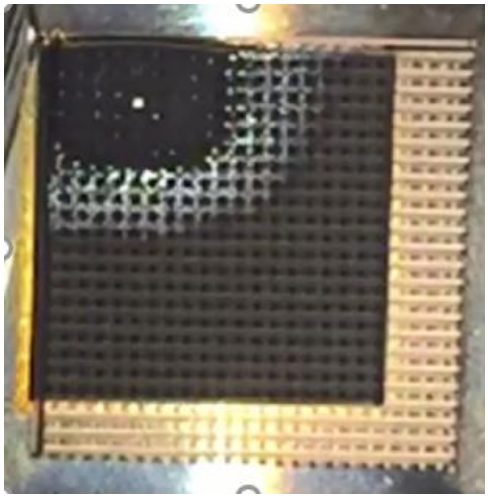

Figure 3.2 Water droplets fall on the FLSP surface showing different wettability.

Another important application of this FLSP surface is it can enhance radiative heat transfer. A FLSP functionalized surface could enhance the heat transfer performance from both pool boiling and Leidenfrost experiments. The self-organized multiscale surface structure increased critical heat flux, heat transfer coefficient, and shifts in the Leidenfrost temperature [31]. Figure 3.3 shows an example of two pots made of stainless 304 steel were used in this study. One pot bottom was processed by femtosecond laser, and the results showed that FLSP pot was boiling was achieved faster than the unprocessed one. As shown in Figure 3.3, there are more bubbles in the processed pot indicating that FLSP enhanced heat transfer.

Figure 3.3. FLSP stainless steel 402 pot enhance radiative heat transfer.

In addition to altering wetting behavior and enhancing heat transfer change, the FLSP also can enhance emissivity [42]. The average emissivity of the unprocessed metal surface is 0.19, while for a processed surface the emissivity can reach 0.67. what's more, the emissivity of a metallic surface can be significantly enhanced through FSLP [42].

3.3 FLSP surface variation and samples used in this study

In this study, a range of multiscale surface morphologies was fabricated on tungsten carbide (WC) and then utilized as the stamps in the next step. FLSP is a one-step fabrication technique that can be used to induce morphological and chemical changes on a metal or dielectric surface. During FLSP, a high peak power femtosecond laser beam (~35 fs) is scanned in a raster pattern across a surface melting and ablating material which results in micron and nanoscale self-organized surface features. A typical FLSP setup used in this work is shown in Figure 3.4. By varying the laser

average power, raster speed, raster pitch, and spot size the self-organized features on the sample can be controlled. For this work, in the stamping part of the research, WC was selected because of its hardness which makes it resistant to wear during stamping and is often used as a machine tool cutting metal. The hardness of WC also makes it difficult to machine with general machine shop capabilities. However a femtosecond laser is able to create controlled micro/nano-scale surface roughness on this very hard material.

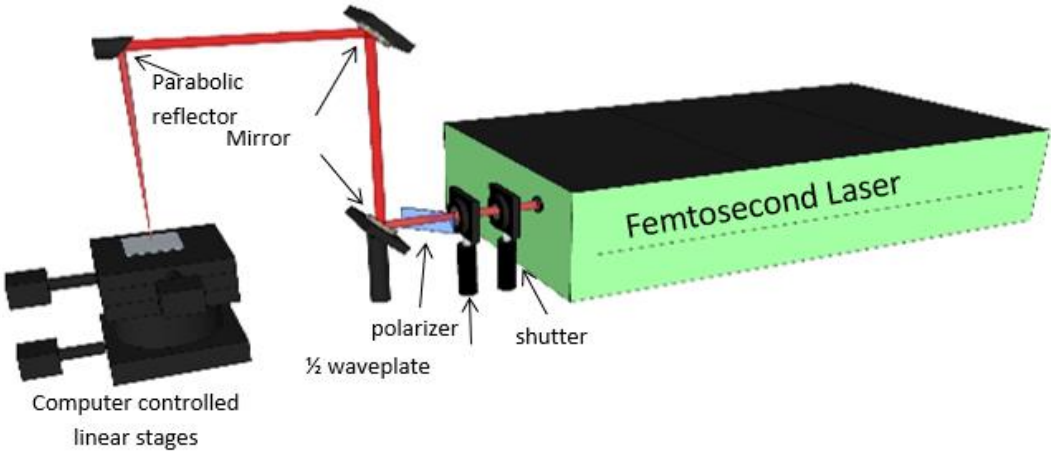

Figure 3.4. Experiment setup for femtosecond laser system.

3.3.1 Variation of FLSP surface

Femtosecond laser surface process (FLSP) can be applied on almost every material. Figure 3.5 shows different surface morphologies of different processed materials. Self-organized surface features have similar repeated surface structures, but the morphology is different from each other. For most metals, for example, sliver, silicon, silicon carbide and stainless steel, they all have a peak-valley mound, while for Al, the surface structure is like a round and mushroom-like mound with nanoparticles covering it. For polymers,

the roughness is less than those on the metals, but the repeated peak structure still can be observed. This technique can be extended to wide range of materials. It can produce multiscale structures in a single step by controlling micro/nanoscale features via laser processing parameters.

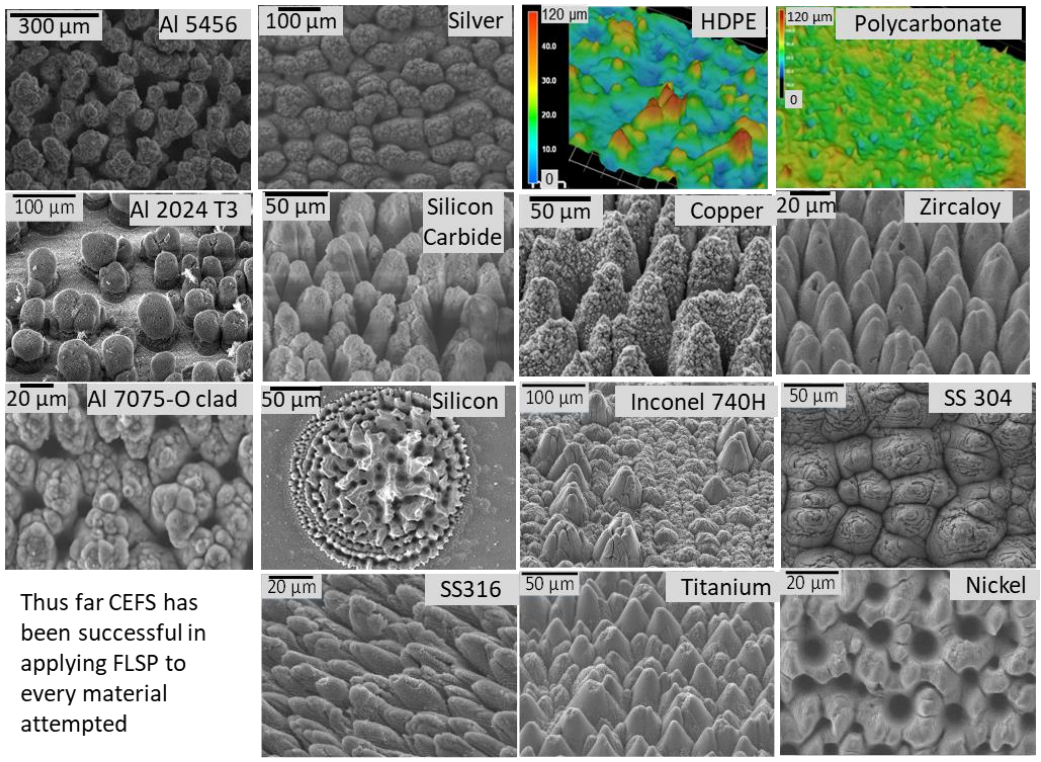

Figure 3.5. Different FLSP structure on different materials

There are three classes of FLSP surface structures produced on the same metal materials: nanostructure-covered pyramids (NC-Pyramid), below-surface-growth mounds (BSG-mounds), and above-surface-growth mounds (ASG-mounds). They are all shown in Figure 3.6. By controlling pulse count and fluence, these surface structures can be obtained by requirement. The NC-Pyramid mounds are formed with laser fluence set between the ablation threshold of the materials. While BSG-mounds and ASG-mounds

are formed with laser fluence much larger than the ablation threshold. But every surface structure is composed by micro-scale peak structures that are covered with nanoparticles. These structures are very different from height, width and the thickness of the nanoparticle layer. All structures growth mechanisms lead to the development of multiscale surface features from surface precursor sites to laser irradiation. Firstly, material is ablated away around a scattering site to form a structure; then, melted materials flows to form structures, and at last particles are redeposited to form structures.

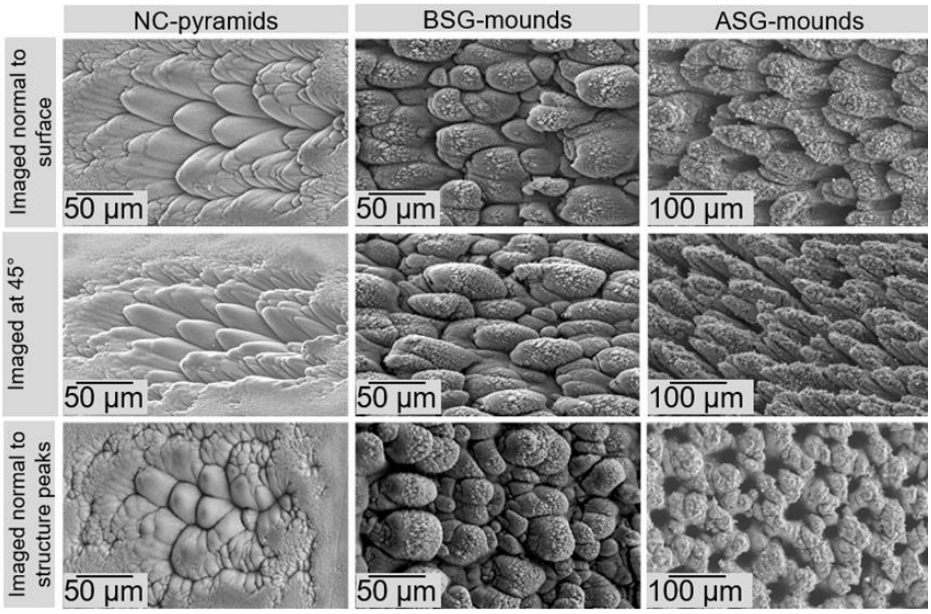

Figure 3.6. SEM images of the three classes of FLSP surface structure.

3.3.1 FLSP Tungsten Carbide

The WC die samples produced were fabricated for the imprint study. The target of the imprint is duplicating the WC die's morphology. In Chapter 5, the detailed surface structure information is illustrated. The application for the WC stamps were in these aspects: 1) investigating the temperature and pressure works for stamping the FLSP

surface structure (Chapter 5); 2) investigating how the morphology of FLSP stamps affect the imprint (Chapter 5); 3) works as the mold for casting (Chapter 6); 4) if the FLSP stamps are strong enough for multiple times stamping (Chapter 8). Figure 3.7 shows the FLSP WC surface structure used in this study.

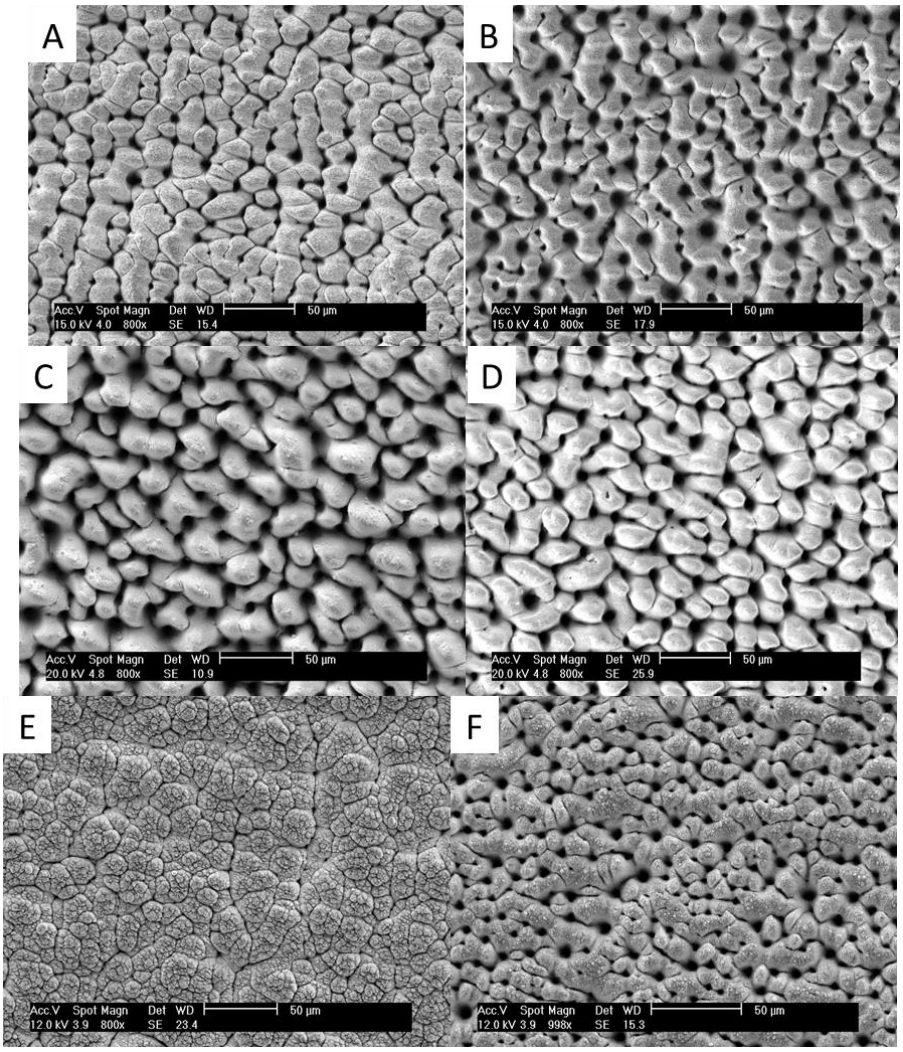

Figure 3.7. Different FLSP tungsten carbide stamps used in this study

3.3.2 FLSP polycarbonate

FLSP also was applied directly to a PC surface to produce a superhydrophobic surface.

An FLSP PC surface was made with a fluence of 0.6J/ cm^2 and PPS (pulses per shot) of 930. A typical CLM image of the FLSP PC sample is shown in Figure 3.8. The detailed morphology information is illustrated in Chapter 7. The FLSP PC was applied to compare the anti-icing property with the imprinted PC sample.

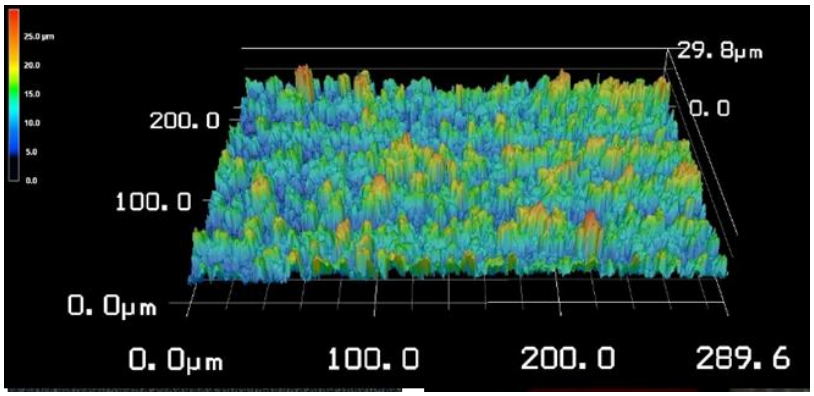

Figure 3.8. Laser confocal microscope scan of the processed PC

Chapter 4. Wetting property

Wettability is directly affected by surface morphology. This chapter introduces basic theory about wetting and the most important application of the superhydrophobic surfaces, as well as how a micro/nano surface structure influences the wetting property. Then, the experimental setup to measure wettability is illustrated. At last, the wetting behavior of the FLSP surface is also presented.

4.1 Review

There are equilibrium contact angles of pure liquids on low-energy and high-energy solid surfaces [33]. Harkins and Feldman concluded that all liquids spread on clean metals and other inorganic high-melting solids have different wetting behaviors by categorized by the spreading coefficients. [34-36], Zisman discovered that soft organic solids with much lower melting points such as waxes and solid organic polymers had specific surface low surface free energies [37]. Liquids usually exhibit nonspreading on those low-energy solids [33]. Then, natural superhydrophobicity attracted the attention of researchers [38]. In many plants, especially lotus flowers, the leaves utilize superhydrophobicity as the basis of a self-cleaning mechanism, as water drops completely roll off the leaf, carrying away undesirable particulates. Since then, researchers have investigated natural superhydrophobic surfaces and attempted to mimic them to produce superhydrophobic surfaces [39].

4.2 Hydrophilic, hydrophobic and superhydrophobic

Before distinguishing different wetting behavior, there are two parameters that need to be introduced first. The contact angle (CA), also called the static contact angle, is the angle between the surface of a liquid and the outline of the contact surface when there is an interface existing between the liquid and the solid. If the surface is flat and smooth, the contact angle can be used to determine the surface free energy of a solid using Young's equation ($\cos\theta = (\gamma_{SV} - \gamma_{SL})/\gamma_{LV}$) [40]. The slide angle (SA) is defined as the angle between the horizontal line and the tilting surface where the water drops roll off, so it is also called the roll-off angle [41]. Contact angle hysteresis is another important element of wetting, it keeps the droplets on the surface. One example is rain drop on a window, gravity pulls on the droplets to move it down, while hysteresis will keep it in place. So, the slide angle reflects the hysteresis between the waterdrops and solid surface. Both contact angle and slide angle are shown in Figure 4.1.

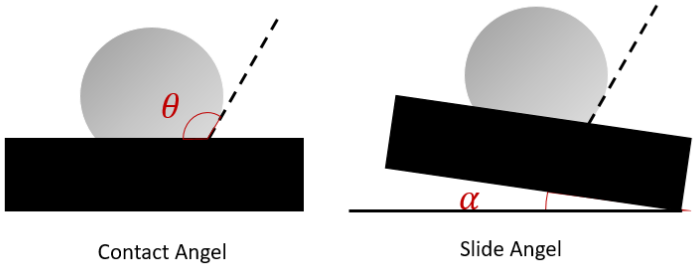

Figure 4.1. Diagram of contact angle and slide angle

4.2.1 Criteria of wetting property

The contact angle defines the wetting behavior, as shown in Figure 4.2. There are three important regions. If the contact angle is smaller than 90 degrees, the surface is hydrophilic, and if it is near 0 degrees it is perfect wetting. On the other hand, if the contact angle is larger than 90 degrees the surface is hydrophobic, if it is larger than 120 degrees it is also called very hydrophobic, and if it is larger than 150 degrees, it is superhydrophobic which is close to a non-wetting state. However, superhydrophobic behavior is properly defined by the slide angle. Slide angles also show the adhesive force between a solid surface and liquid. From nature, lotus leaves have a high contact angle and a low slide angle, so water can roll off of its surface. While the rose flower surface also has a high contact angle, it does not have a self-cleaning function, because it has a high slide angle [42-46].

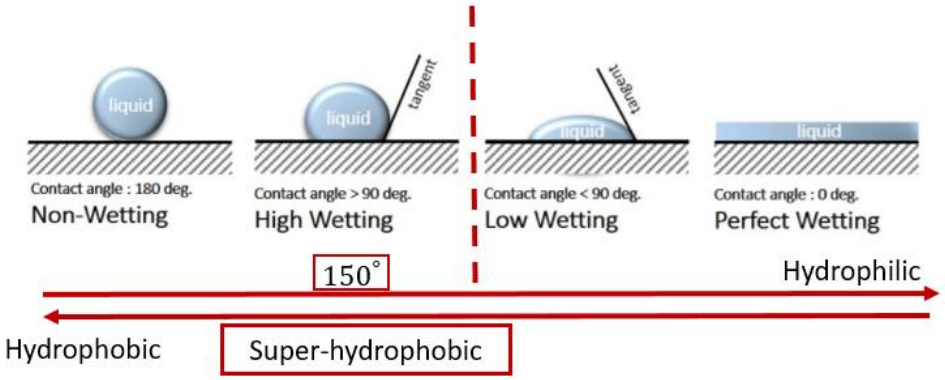

Figure 4.2. Distinguish different wetting properties by contact angle

4.2.2 Young's equation

Young's equation shows the equilibrium between the liquid and solid surface.

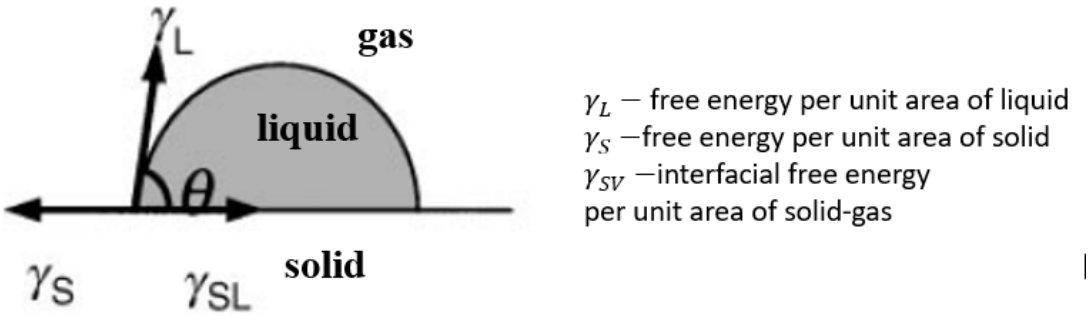

Figure 4.3. Diagram of different phase and contact angle.

γ_{SV}, γ_{SL} and γ_{LV} are the interfacial free energies per unit area of the solid-gas, solid-liquid and liquid-gas interfaces. This equation is only applied to flat surfaces.

$$\cos\theta = (\gamma_{SV} - \gamma_{SL})/\gamma_{LV}$$

From Young's equation, it can be concluded that if attempting to improve the hydrophobicity of a flat surface, the only method that can be used is lowering surface energy.

From the publications the lowest surface energy value recorded is 6.7 mJ/m^2which is from the surface with regularly aligned hexagonal close-packed CF_3 groups [47], the maximum contact angle can be calculated to be $120°$ [47-50].

4.3 Different wetting property by rough surface

Young's equation is a general equation that assumes the solid surface is flat and smooth. If there is surface roughness or tailored topography, there are two different states of the liquid-solid interaction: the Wenzel state and Cassie-Baxter state [51,52].

Two other models are applied to explain the equilibrium between each phase [52]. The

Wenzel model and Cassie model are illustrated below.

4.3.1 Wenzel model

When a liquid droplet is introduced onto a solid surface, it spreads until a specific contact angle is attained, depending on the surface tension of the solid-liquid, solid-air and liquid-air interfaces. In one state, a droplet of liquid immerses into the surface texture, eliminating the air-liquid interface against the surface as shown in Figure 4.4. Wenzel [53] suggested that if liquid contact followed the contours of a rough surface then the effect of roughness should be to emphasize the intrinsic wetting tendency towards either film formation or enhanced contact angle. The contact angle observed is given by Wenzel's equation.

$$\cos\theta' = \frac{r(\gamma_{SV} - \gamma_{SL})}{\gamma_{LV}} = r\cos\theta$$

where θ' is the real contact angle, r is roughness factor, defined as the ratio of the actual area of a roughness surface to the geometric projected area.

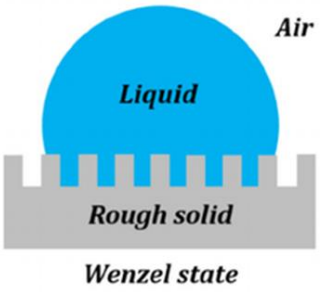

Figure 4.4. Diagram of Wenzel state

4.3.2 Cassie-Baxter model

Opposite to the Wenzel state where a droplet of liquid immerses into the surface texture, in the Cassie-Baxter state it rests upon the surface texture. Here, liquid bridges across the tops of surface features so that the droplet rests upon a composite surface features, so that the it rests upon a surface of the flat solid tops and flat air gaps between them [54]. In the Cassie-Baxter model, the contact angle is given by,

$$\cos\theta' = f\cos\theta + (1-f)\cos 180° = f\cos\theta + f - 1$$

Where f is solid surface area fraction, defined as $\frac{\sum a}{\sum a+b}$, θ is the ideal contact angle assuming the surface is flat, θ' is the real contact angle,

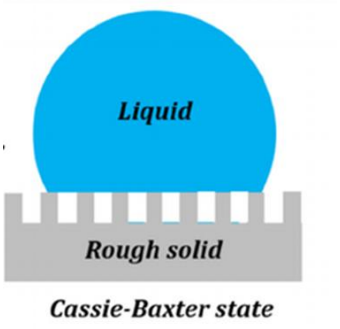

Figure 4.5. Diagram of Cassie-Baxter state

The two models can be combined to produce a more general model to cover the case when the contacting areas themselves are not flat. From these models, it can be concluded that in order to improve hydrophobicity of a solid surface, there are two general methods: decrease the surface energy or increase surface roughness.

4.4 Experimental setup used for wetting property measurement

The wetting behavior was quantified by contact angle in this study. The contact angle was measured using droplet tests. All droplet tests were conducted by remé-hart® advanced automated goniometer/tensiometer with DROPimage Model 590. DI (de-ionized) water was used to produce the liquid drops. For each sample, three test spots were selected. Each droplet had 5.0 μl. Static contact angles (CA) have direct relationship with the flat surface's wetting behavior. The CA were used to quantify the wettability of the samples.

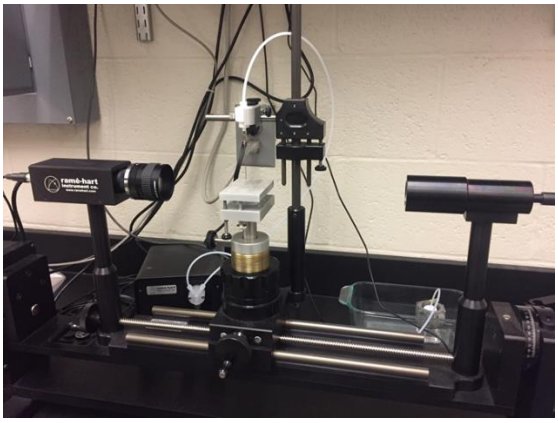

Figure 4.6. remé-hart® advanced automated goniometer/tensiometer for droplets test

4.5 Patterned FLSP surface structure affects wetting behavior

Before measuring the imprinted FLSP surface, the FLSP stamps' wetting behavior was measured to characterize the original morphology.

As seen from Figure 4.7, most metal material surfaces became hydrophilic with a

contact angle close to 0 degrees after FLSP. Their surface was so hydrophilic that water droplets immediately spread out as soon as they contacted the sample surface.

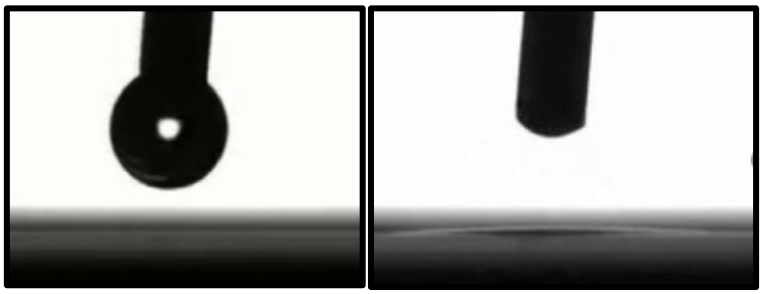

Figure 4.7. Hydrophilic FLSP metal surface

While after the O-ring siloxane deposition (a type of deposition to lower surface energy), the wetting behavior of the FLSP surface became so different from before. The surface became superhydrophobic with a contact angle close to 150 degrees. This is a phenomenon for nearly all FLSP metal material. It is assumed that since the surface morphology has been changed, with a high surface energy, the self-organized surface morphology led to the Wenzel state. After siloxane deposition, the surface energy decreased by this process, so it leads to the transformation from the Wenzel state to the Cassie-Baxter state.

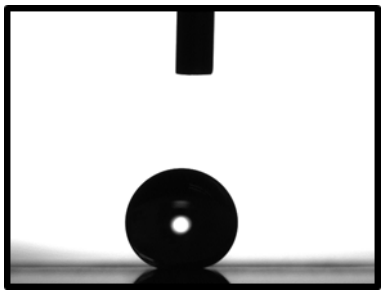

Figure 4.8. Superhydrophobic FLSP surface

Detailed descriptions about FLSP surface are in Chapter 5.

Chapter 5. Imprint FLSP surface for general application

A variety of experiments were conducted to explore the feasibility of duplicating the FLSP surface structure by stamping method. These experiments have been divided into two groups by blank materials-metal and polymer. This chapter gives a detailed description about the stamping environments' influence on the imprint quality and wettability.

5.1 Introduction

Stamping is a commonly used manufacturing process as it has many advantages, including high productivity and relatively low assembly costs. Worldwide, manufacturers have attempted to apply and improve stamping to reduce costs and processing times [55,56], from which many new technologies, such as high-speed milling and stamping lubricants, were developed. As mass production of micro/meso-size features became a requirement, especially in the electronics industry, microforming began to attract the attention of scientists, beginning with Meada's proposal to develop a microprecision press machine in 1990 [57,58]. The modeling of stamping using an FLSP surface has not previously been studied, although a number of papers have been published on nano-indentation.[59-62] Studies on the geometric effect of the indenter tip on different materials have reached different conclusions. The geometry of the

indenter tip does not have an effect on the load-displacement relation according to an FEM simulation study by Li et al. on the four different kinds of indenter tips. This conclusion was confirmed by Swaddiwudhipong et al, in their simulation on 6061 aluminum [63]. An investigation by Xu and Li determined that the geometry of the nanoindenter had a different effect depending on the samples' hardness [63]. Moore found that there was an obvious difference in the load-depth curve when considering the isotropic and kinematic hardening of 6061 aluminum [64].

The "positive" micro/nanostructures used as the die in the model were produced by FLSP, and a relatively softer material was used as the blank. The duplication of the FLSP surface morphology is significant in reproducing functionalized surfaces and can greatly decrease the amount of processing time.

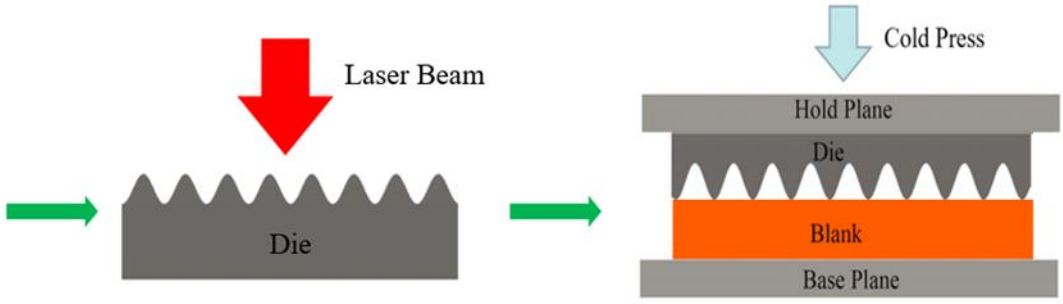

Figure 5.1. Imprinting using an FLSP surface. First, the femtosecond laser beams generate the positive mounds (die) on a hard material (left). Then the positive surface is used as the die to press a piece of relatively softer material (blank), keeping the materials between two holders. By increasing the press load, the negative surface on the blank (right) is generated.

5.2 Finite elemental model

Finite element (FE) simulations were performed to better understand the imprinting process of FLSP surfaces. The first process to be modeled was a single-mound

imprinted on the blank body. The model was divided into two parts to investigate the effects of the die geometry and blank material separately. Finite element analysis (FEA) was performed using ABAQUS 6.12.

During the imprinting process, the die was assumed to be a rigid body, and the blank was OFC, which was treated as a typical elastic-plastic material.

The criterion for quality imprinting is the stress-displacement relationship of the blank during the imprint. Die geometry and the effect of the properties of the blank material were compared using several models. The control parameters of the die geometry were roughness, R_Z, (height from peak to valley), and period (the distance between two mound peaks). Stainless steel (304SS) was the material used for comparison with oxygen-free-copper (OFC). All simulations were divided into two groups. The material and geometry effects studied are illustrated in Table I and Figure 5.2.

Table 5.1. Input parameters to investigate the effect of imprint material and die geometry.

	Materials		$R_{Z/}$(μm)	Period (μm)
Group 1 (Material effect)	304 SS		50	100
	OFC		50	100
Group 2 (Geometry effect)	Subgroup 2-1	OFC	50	100
		OFC	100	100
	Subgroup 2-2	OFC	50	100
		OFC	50	25

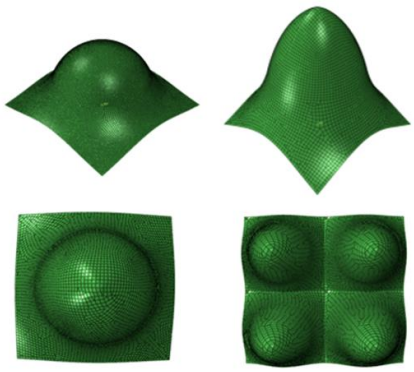

Figure 5.2. The illustration of the models with different roughness (top row) and period (bottom row).

5.2.1 Material influence

As expected, the simulation showed that OFC is easier to imprint than SS 304 (see Fig.5.3), especially in the large displacement regions. When the die starts to penetrate into the blank samples, the stress needed for the SS 304 and OFC is similar, up to 300 MPa. Then as the die tip penetrated deeper, the two metals had different stress

requirements. The difference in displacements between the two materials at elevated stress levels was primarily due to the difference in the plastic properties of the two materials.

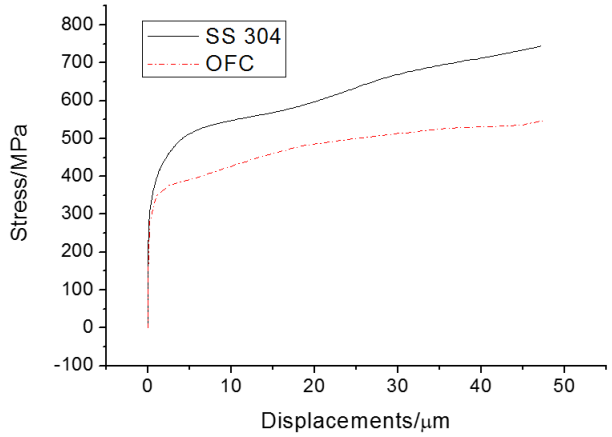

Figure 5.3. Simulated stress-displacement relationship between 304SS and OFC

5.2.2 Geometry influence

Figure 4.4 illustrates how the die geometry (roughness and period) affected the stress-displacement curve. A higher stress is needed to imprint surfaces with higher roughness. A larger stress is needed for the imprint as the period between structures decreases (i.e. a larger density of mounds). A larger difference was observed when the indentation depth was considered, and it was more significant for structures with smaller periods. The roughness-to-period ratio (referring to the peak-to-valley height and the peak-to-peak distance) is an important parameter in a cone's morphology. It is often used as an index in determining morphological effects [65-67]. Describing all of the models by the value of the roughness-to-period (reflected by the height-to-radius ratio for a single mound), the values were second and eighth in the period group, and second and fourth

in the R_Z group. The order of the height can be reflected by the stress-displacement curve: the larger the mound roughness-to-period ratio, the harder it is to imprint.

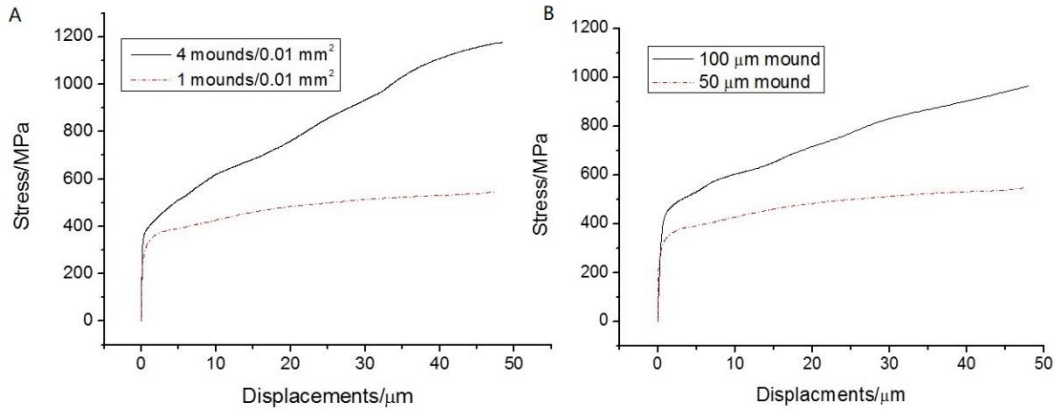

Figure 5.4. Stress-displacement relationship of the imprint models with different die geometries. (A) The left plot shows the difference between different mound periods, indicated by the density. (B)The right plot shows the difference between different mound heights.

A different roughness-to-period ratio can also be reflected by the stress focus area. The high roughness-to-period ratios mound, which was sharper, had a larger stress focus area. Figure 5.5 is a comparison of blank stresses in the focus regions of the roughness subgroup. It also explains why, for imprints at the same penetration depth, the sharper dies need more stress to imprint.

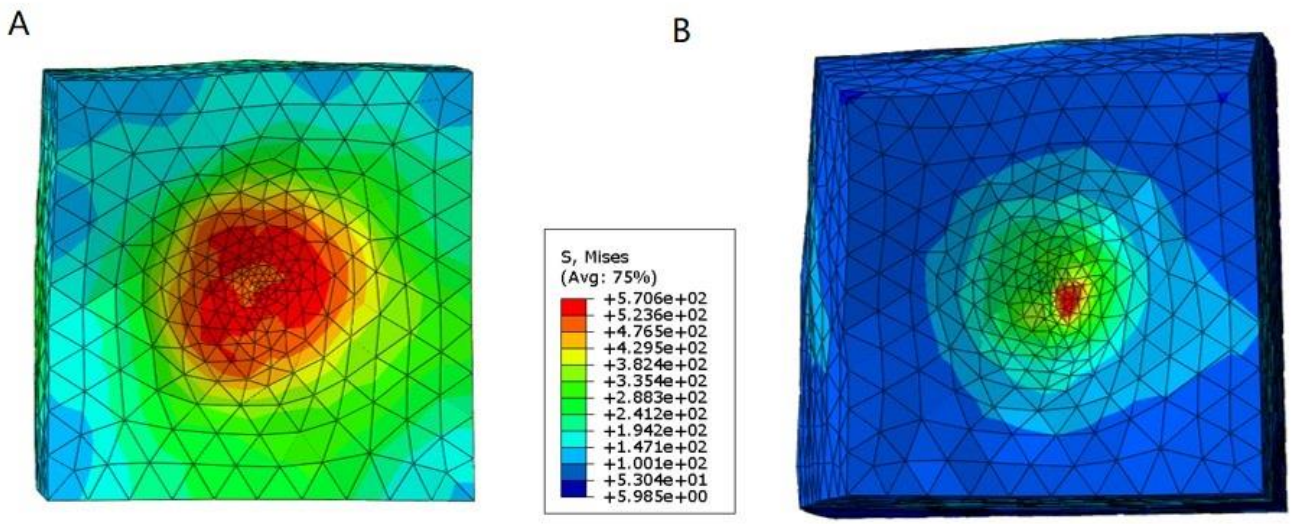

Figure 5.5. Stress distribution of the 50 and 100 μm (right) mound imprint when penetration goes to 50 μm.

5.3 Imprint FLSP surface to metal surface

The metal stamping technique applies dies and punches to press the metal into the desired shape of the die. Stamping or imprinting is one of the conventional techniques widely used in the manufacturing field due to its advantages of mass-production [68]. If replacing the die with the FLSP surface, the negative FLSP surface pattern should be imprinted in the counterpart surface. With the imprinted FLSP surface topology, the wetting property of the counterpart surface is assumed to be different from the one imprinted previously, and it will be consistent with the FLSP die surface. The single mound's simulation result showed that the die's morphology and blank materials will influent the imprinting quality [69]. In this simulation work the die was assumed to be rigid, so the selection of the die materials should be hard enough to stamp the blank material without much degradation. This experimental study fixed the die and blank materials to be FLSP Tungsten Carbide (WC) and Aluminum (Al) 1033, respectively,

investigating the wetting property variation by different blank morphologies caused by different pressure and temperature. The before and after image of the die surface morphology also could be observed.

5.3.1 Pressure influence

To investigate the pressure influence during the imprint, a series of experiments was conducted. The die and blank material are Tungsten Carbide (WC) and oxygen free copper (OFC), respectively.

The stamping experiments were conducted in air at ambient temperature, and the loads applied on the samples ranged from 2.5 ton to 12.5 ton, which corresponded to 245 MPa to 1225 MPa considering the sample area. While, it should be noted that the pressure showed above is not the real pressure working on the mounds, the real contact area of the stamping process was different than $1 \times 1\ cm^2$, due to the mound's penetration area always varying by indentation. The separation was operated after 5 minutes.

During the cold imprint, the roughness of the negative increased with the increased loads. However, the morphology of cold stamped surface morphology are more likes pits than the mounds. As shown in Figure 5.6, under 2.5, 5, 7.5, 10 and 12.5 ton's loads, the roughness of the imprinted OFC surface was $30.4 \pm 5.8, 36.5 \pm 3.4, 40.5 \pm 5.1, 40.3 \pm 5.0, 40.8 \pm 4.3\ \mu m$ for the different loads. The pit depth and radius increased with increased pressure.

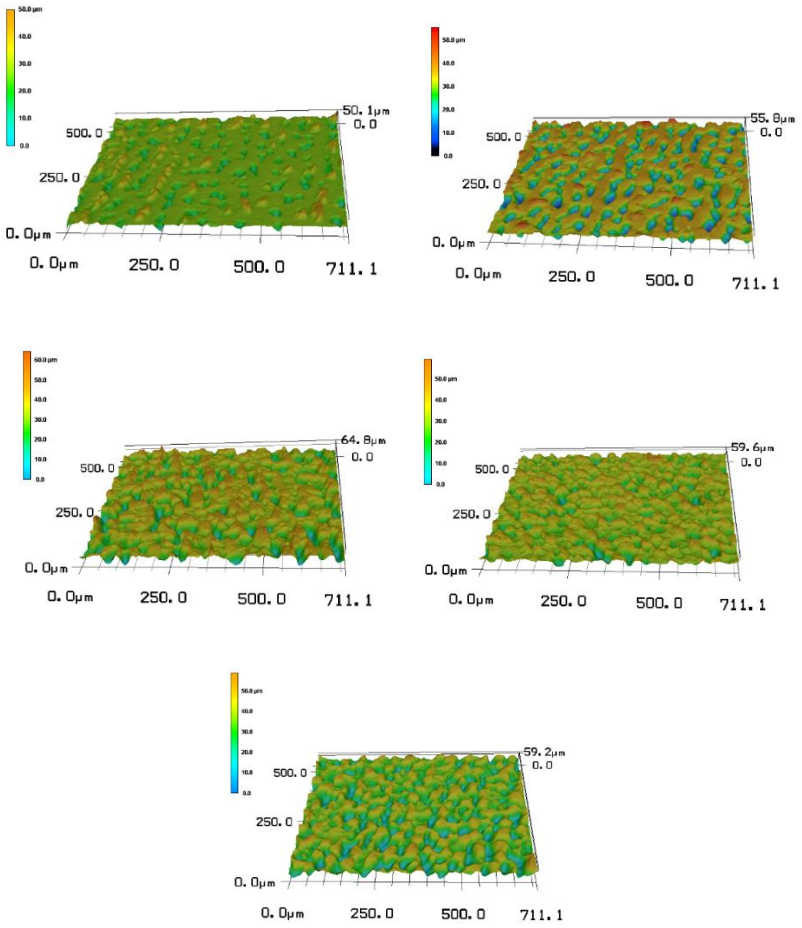

Figure 5.6. OFC's 3D morphology varies with the increased pressure during cold stamping, the peak-to-valley heights $\boldsymbol{R_z}$ are $\mathbf{30.4 \pm 5.8, 36.5 \pm 3.4, 40.5 \pm 5.1, 40.3 \pm 5.0, 40.8 \pm 4.3\ \mu m}$ for load 2.5, 5, 7.5, 10 and 12.5 ton, respectively

5.3.2 Temperature influence

The die and blank used in the imprint process were the featured WC surface and flat Aluminum 1033, respectively. Twenty FLSP WC samples were divided into four groups by operating pressure and temperature, which were 3 and 6 ton (294 and 588 MPa) and room temperature (cold stamping) and 300 ℃ (hot stamping). During hot stamping, the temperature increased to 300 ℃. After the imprint was done, it cooled down for five minutes. Then, the compressed samples were separated to get the imprinted Al surface.

The Al samples used as the blank were 1033 Al, with a Mohs hardness scale ranging from 2~2.9. The melting temperature of aluminum is 670 ℃. After imprinting by different pressures and temperatures, Al samples showed different morphological characteristics. As shown from Figures 7 and 8, under room temperature, a low load (3 ton) resulted in shallow pits on the Al surface. As loads increased, pits were deeper while the regions between the pits were still relatively large and flat. By increasing the temperature to 300 ℃, even the load applied on the surface was low (3 ton). The patterns on the Al sample still were clear and deep, and the regions between the pits were smaller and smaller, developing into peak regions. This trend was more obvious under high pressure, the flat regions became so small that they became a relatively sharp topology. The roughness comparison between different samples. R_P refers to peak height, R_V refers to valley height, R_Z refers to the peak-to-valley height are shown in Figure 5.7. According to this comparison, the peak-to-valley height, R_Z, of Al C6 (82 ± 6 μm), Al H3 (83 ± 9 μm) and Al H6 (85 ± 10 μm)all have similar values compared with the FLSP die surface. However, both Al H3 and Al H6 samples' peak height. R_P, is larger than the valley height, R_V, while the Al C6 and FLSP die surfaces show the reverse. The hot imprinted Al samples' surface also are more consistent with the negative FLSP surface as seen in Figure 5.7.

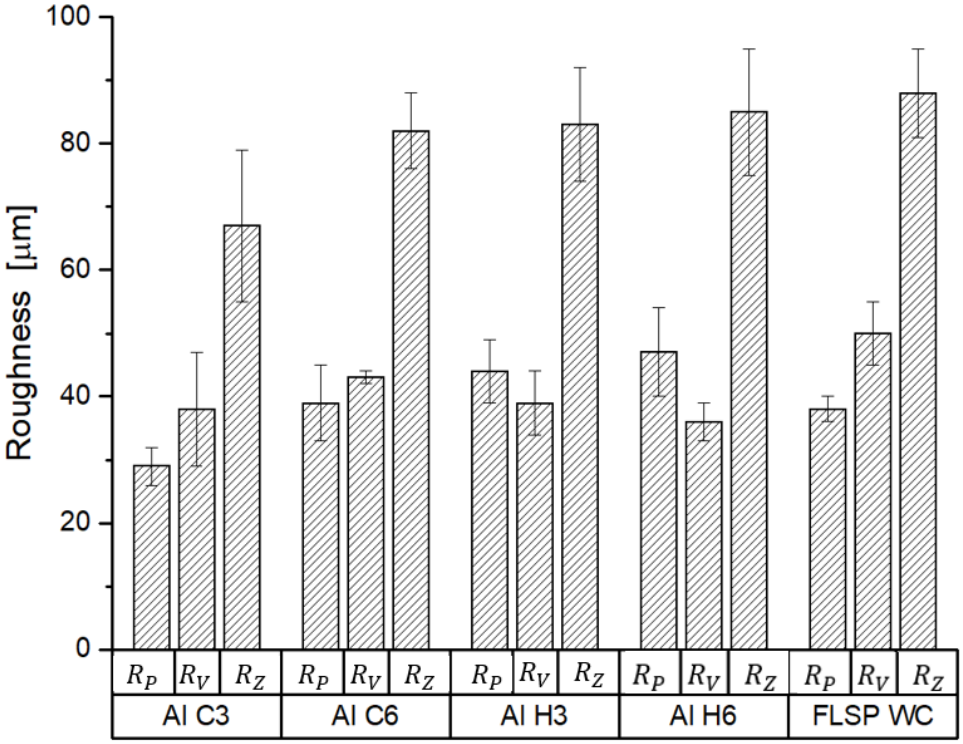

Figure 5.7. Roughness comparison between imprinted Al samples and the FLSP WC die. Al C3 are Al samples imprinted under 3 ton, room temperature, Al C6 are imprinted under 6 ton, room temperature; Al H3 are imprinted under 3 ton, 300 ℃, Al H6 are imprinted under 6 ton, 300 ℃.

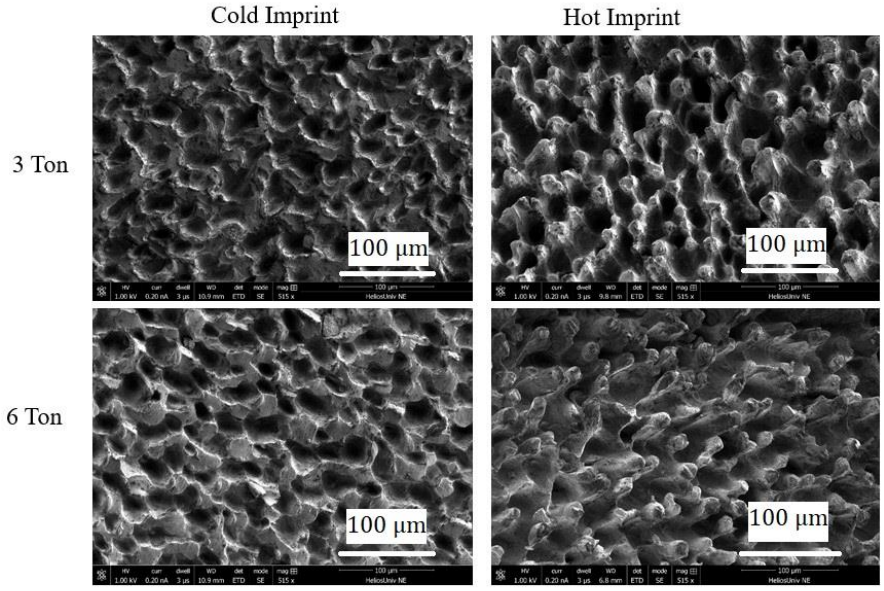

Figure 5.8. Al sample morphology after imprint by the FLSP WC die under different

conditions

Before the imprint, the polished Al sample surface had an average static contact angle of $84.1 \pm 2.4°$. Al samples imprinted at room temperature (Al C3 and Al C6) showed wetting behavior more hydrophobic than before, with the average contact angle measured to be $128.7 \pm 9.8°$. The Al alloy wetting behavior as a function of stamping method is shown in Figure 5.9. Hot stamped Al samples' wetting behavior is consistent with the FLSP WC surface, where the "negative" surface geometry come from. As with the FLSP WC, the hot stamped Al alloy surface behaves super hydrophobic after deposition of siloxanes from VMQ (a group of elastomeric materials) O-rings. Both surfaces repelled water drops when water drops touched the surface. This was not observed for the siloxane-coated flat Al alloy sample.

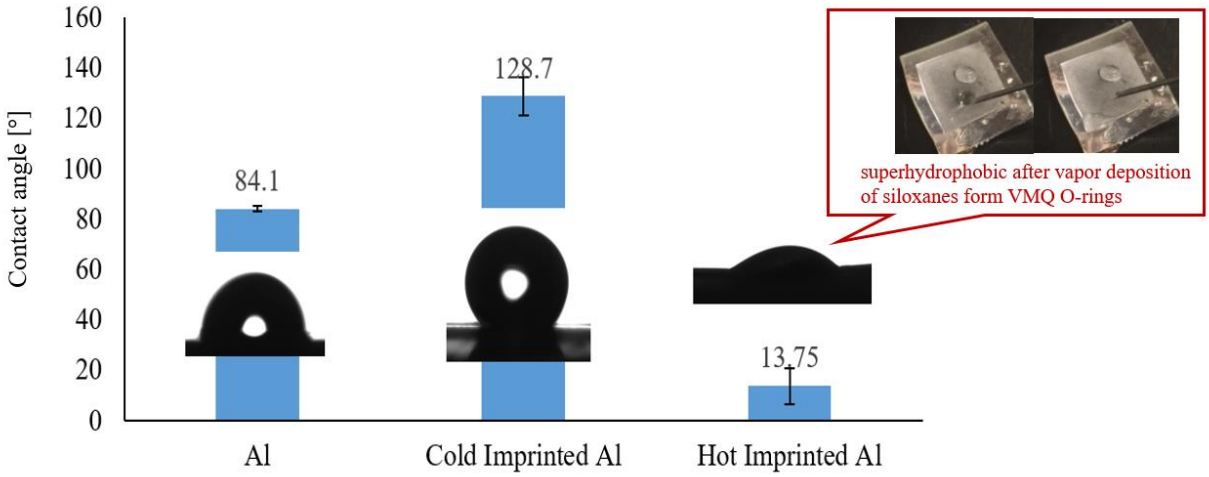

Figure 5.9. Contact angle comparison between different Al samples

5.4 Imprint FLSP surface to polymer surface

Polymer materials are another blank material used in this research. Polycarbonate is one of the commonly used traffic signal lens material. It is assumed that after stamping,

with similar morphology of the FLSP surface, PC surface becomes more hydrophobic. With more hydrophobic surface, the traffic signal lens keeps being visible for drivers thus to reduce traffic accident in cold and ice weathers. It is even more significant for railway traffic signal lens with larger areas.

Tungsten Carbide (WC) and Polycarbonate (PC) used as railway traffic signal lenses were applied as the templated die and blank materials, respectively. WC material is an extremely hard material with a Mohs hardness scale 8.5-9.5 (Diamond being 10.0) [70,72], comparing with PC, FLSP WC should be strong enough to be the die. So, it was applied the die in the experiments.

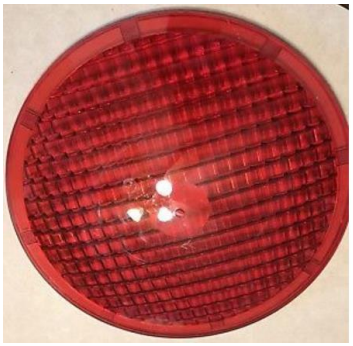

Figure 5.10. Red railway traffic signal lens (polycarbonate) used as blank material in this study

The imprint process is the key process that duplicates the FLSP surface structure onto another materials surface. The stamping process is a traditional manufacturing process, it has an economic advantage compared with FLSP. The patterned surface produced by FLSP was used as the die in the stamping process. Since WC is a hard material with a Mohs hardness number of 8.5-9.5, the FLSP surface is assumed to be similar in the

hardness. While PC is a soft material with a Mohs hardness scale number 3, during stamping the patterns on the WC sample pieces will be imprinted on the PC surface. Figure 5.11 illustrates the imprint process. Stamping was accomplished using a CARVER®, model 2699 with a load range of 0-15ton. During the stamping, one custom-made steel holder was used to keep the force even.

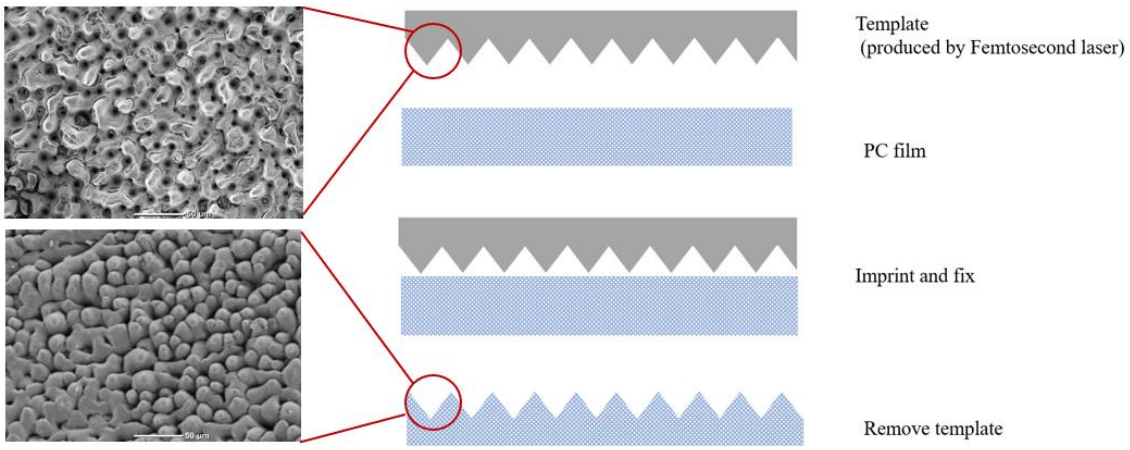

Figure 5.11. Imprinting using an FLSP surface. First, the femtosecond laser beams generate the die's template on a piece of Tungsten Carbide (WC) block. Then the template presses on the Polycarbonate (PC) film, applying load and heat during the imprint; removing the template then gets the negative patterned PC film.

The WC surface was patterned by FLSP. Then the FLSP WC surface was pressed on the PC surface at different temperatures and pressures. The droplet test was conducted immediately after cleaning the PC surface in an ultrasonic bath. The FLSP, imprint process, and droplet tests are detailed separately. The KEYENCE laser confocal microscope was used to observe and measure the surface roughness. The scanning electron microscope (SEM) was used to observe the morphology of the imprinted surfaces.

Figure 5.12. CARVER® model 2699, compression machine for the stamping, right bottom shows the stamp holder.

5.4.1 Influence of temperature

Temperature is one of the two key factors that will affect the imprint results. Since polycarbonate has a glass transition temperature of about 147 ℃ and a melting point of around 200 ℃ [72-74]. Firstly, set the work temperature between 50~200 ℃, with the interval be 50 ℃, four identical FLSP tungsten carbide stamps compress on four polycarbonate samples ($1 \times 1\ cm^2$). The work temperature is 50℃, 100℃, 150℃ and 200 ℃ separately. Then the set the work temperature between 120~140℃ (This range is dependent on the combination of difficulty of separating the die-blank samples and the curvature of the polycarbonate surface), the interval be 5℃.

Four typical surface structure of the imprinted PC surface are shown in Figure 5.13. These SEM results showed that the surface morphology changed greatly from 100~150℃, varying from a pit-like structure to a mound-like structure. Under 50 ℃,

the PC samples' mechanical property should be similar to the room temperature. With a larger pressure, only the taller mounds penetrated into the PC surface, so the morphology of the PC showed pit-like structures. As the temperature increased, the PC became softer, and since the load was fixed, more mounds could be imprinted on the PC surface, while still being pit-like under 100 ℃. While when the temperature reached above 150 ℃, which is above PC's glass transition point, the PC's mechanical property largely changed to rubber-like material, so at 150 ℃, the surface showed shallow mound-like structures. At the stamping process, the PC largely sprang back due to the change of material property. At 200 ℃, for the PC material, it already reached its melt point, the surface showed good mound-like structures. During this process, the PC had already been melted. When it was cooled down, the imprinted PC mounds were the re-solidified materials. Considering the glass transition temperature of PC is 147 ℃, smaller intervals should be applied to study temperature influence.

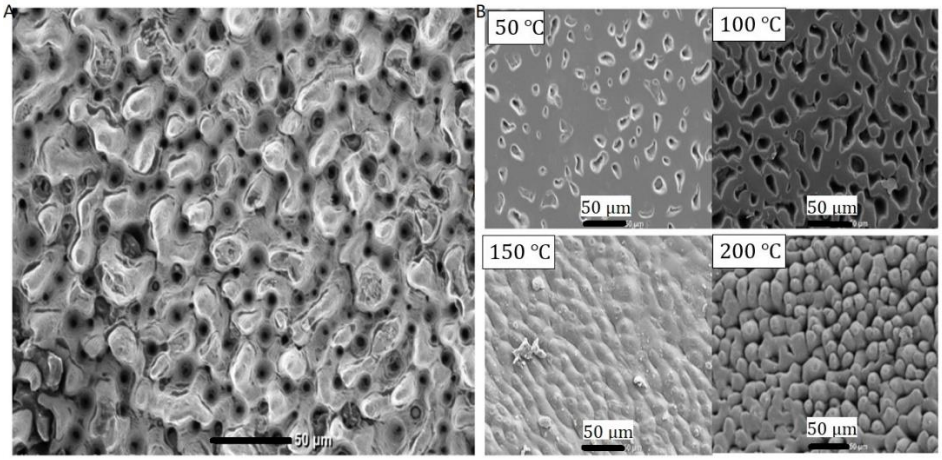

Figure 5.13. Different morphologies of the imprinted PC. Left: SEM of the FLSP WC surface as the die; Right: four typical morphologies of the imprinted PC surface.

Although the surface structure at 200 ℃ looked desirable, the sample twisted too much due to the high temperature. The twisted surface introduced great difficulties in roughness measurement and droplets testing.

In this experiment, the temperature range turned to be 120 ~140 ℃, with 5 ℃ intervals. The results indicate that during this temperature range, the PC had the best imprint quality reflected by the peak-to-valley height (44 μm) at 120 ℃, as well as wetting property reflected by the contact angles (115 °).

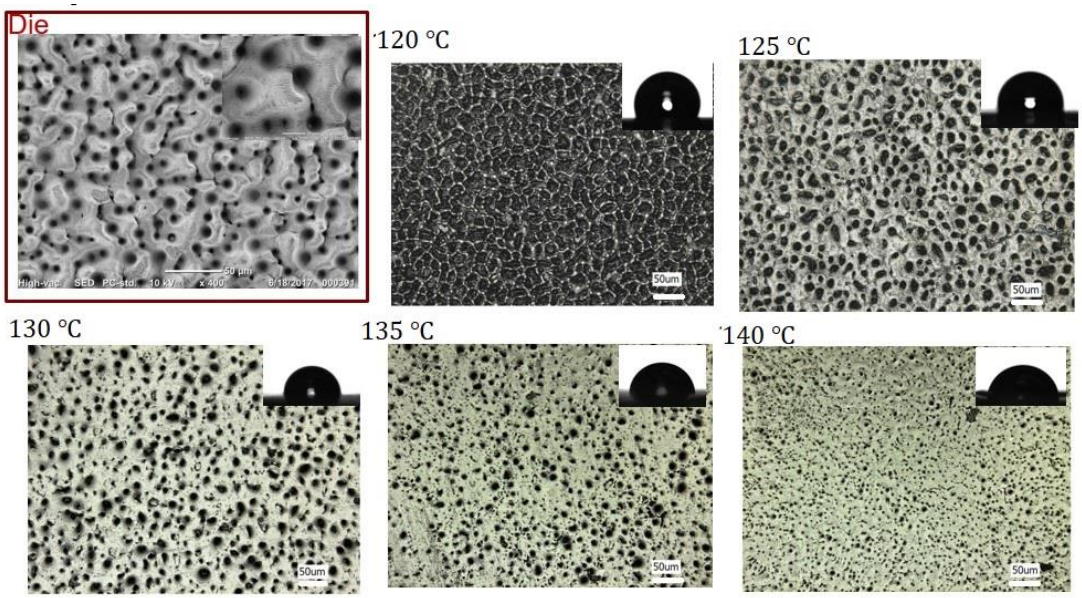

Figure 5.14. Different PC surface morphologies by different stamping temperature with fixed pressure, from 120℃~140℃.

The peak-to-valley distance roughness, R_z, was used to quantify the imprint quality. Figure 5.14 and Figure 5.15, show the morphology and R_z, and it can be seen that R_z reaches its peak value 36 ± 10 μm at 120℃. Compared with 50 ℃ and 100 ℃, the R_z from 120℃ largely increased. This is because the mechanical property had changed largely under 120℃. The PC under 120℃ was much softer than the one

under lower temperature. While R_z at temperatures $125, 130, 135, 140$ ℃ also was smaller than it was under 120℃, indicating that when the temperature was larger than 120℃, the mechanical property of the PC changed to a rubber-like property, so after compression it would spring-back to its original state, the higher the temperature (until 140 ℃), the more it would spring back. So 120℃ should be an ideal temperature to conduct the stamping process on railroad traffic lenses using PC.

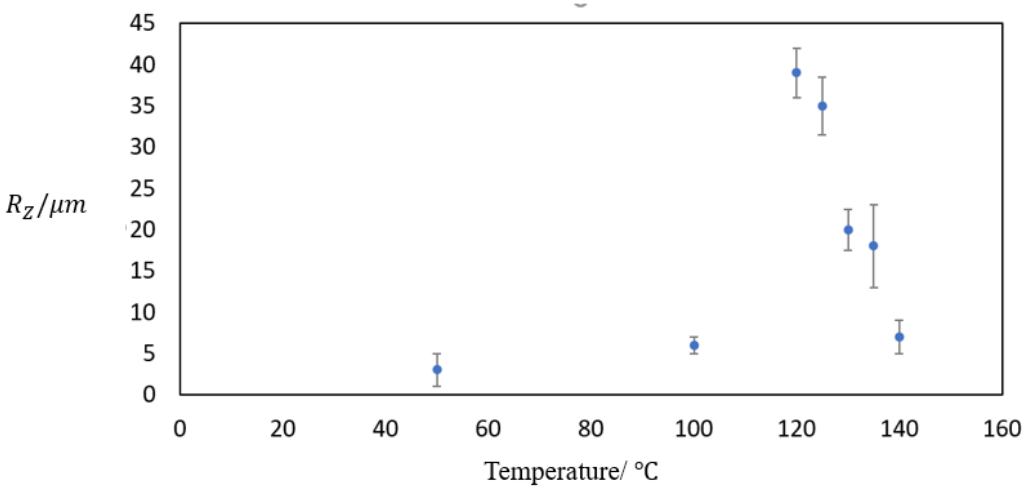

Figure 5.15. Peak-to-valley height of PC surface by different stamping temperature with fixed pressure, from 50℃~140℃.

The wetting property variation is consistent with the peak-to-valley height variation. The highest contact angle, $115.1°$, occurred at 120℃. It indicated that R_z was one of the factors that determine the surface wetting property. However, it was still not superhydrophobic. Compared with the FLSP surface, the imprinted surface, R_z, was nearly half of the FLSP tungsten carbide die, which was $83 \pm 6\ \mu m$. This result indicated that PC material surface varies by the surface roughness R_z, and the highest contact angle of the PC surface has the highest peak-to-valley height.

5.4.2 Influence of pressure

A key factor in the environments that will affect the imprint quality is load. This experiment was designed to investigate the loads effect, so the temperature was fixed at $120\ ℃$. The load of the compression was interpreted into the displacement by the machine. Four identical FLSP tungsten carbide stamps compressed on four polycarbonate samples ($1 \times 1\ cm^2$), the work temperature was set to be $120\ ℃$ by the furnace, while the compression distance was $0.1\ mm, 0.2\ mm, 0.3\ mm$ and $0.4\ mm$, respectively.

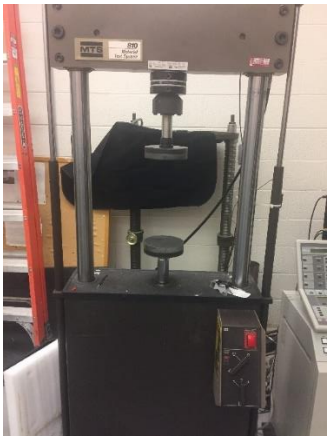

Figure 5.16. MTS 810 material test system for stamping

A displacement-controlled compression machine was used in this research. Unlike the experiments which varied pressure and temperature, this experiment was controlled by the overall PC sample's displacement.

Displacement reflects the load from variation, by the morphology of the imprinted PC surface and the peak-to-valley roughness, R_z, there is little difference between the 0.1, 0.2, 0.3, 0.4 mm displacement PC surfaces, However, these were different in the

morphology of these surfaces. For the one compressed 0.1 mm, the peaks completely formed between the valleys, and thus the surface morphology was more like the mound-like structure, while for the 0.2, 0.3 and 0.4 mm sample surfaces, the regions between the valleys were relatively flat compared to the 0.1 mm sample surface. The droplet test also showed that those mound-like structures played a role in improving the surface wettability, with a contact angle of 130°.

The results showed that the surface displacement was not consistent with the sample bulk's displacement. It had the best imprint quality and wetting property at the 0.1 mm displacement.

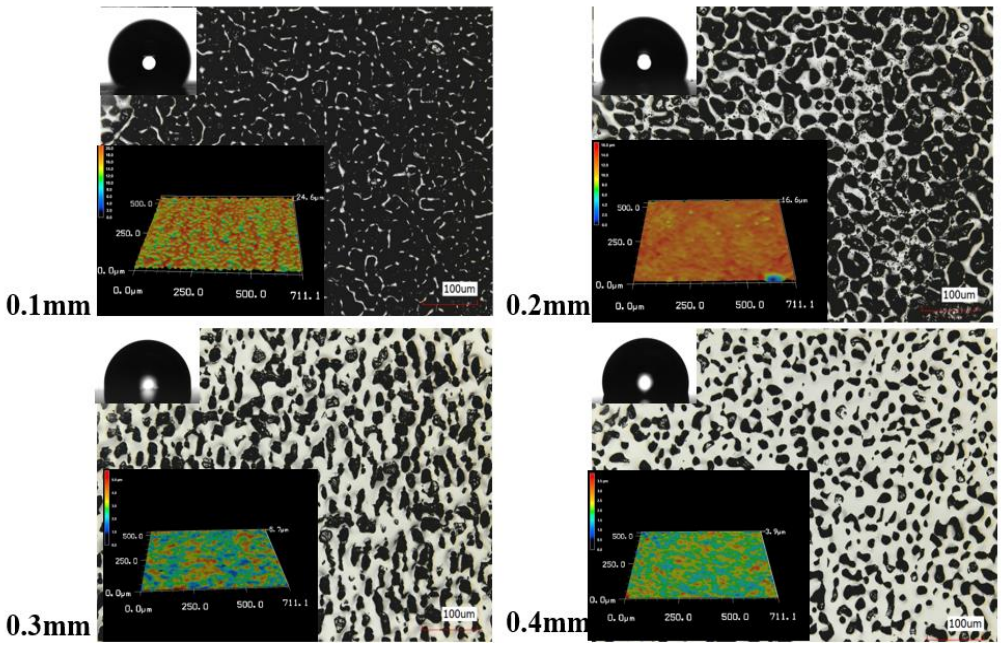

Figure 5.17. Different PC surface morphology by different stamping displacement with fixed temperature (120℃), from 0.1~0.4 mm.

5.5 FLSP surface morphology's effect on the imprinted PC surface

In the previous section, the conditions to transfer the micro/nanostructure from the die onto a PC surface had been explored, and the FLSP surface morphology's influence on the PC surface morphology and wetting behavior was studied.

The approach was to vary specific surface features as independently as possible and evaluate the properties. The pairs of dies made varied in roughness, peak-to-peak distance, and structure type. Listed in Table 1 are the FLSP parameters that were used to create the WC samples. SEM images and other relevant data about the surface morphology were discussed. Mound roughness influenced imprint morphology.

TABLE 5.2. FLSP parameters used to produce the samples discussed in this report, PPS means pulses per spot

SAMPLE	FLUENCE (J/CM^2)	PPS
A	**70.7**	**196**
B	**1.9**	**1211**
C	**53.1**	**295**
D	**53.1**	**196**

E	**0.4**	**844**
F	**2.8**	**1021**

The literature indicates that roughness has a large effect on wetting behavior [75-80]. With that in mind, we produced stamps with different roughness while maintaining very similar structures. SEM images are shown in Figure 5.18. Samples A and B have an RMS surface roughness of 4.03 and 4.82 microns, respectively, as determined using LSCM.

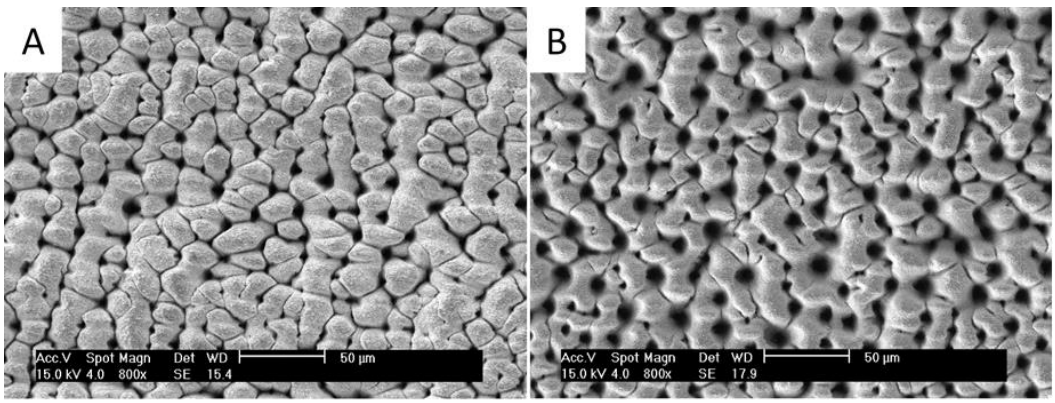

Figure 5.18. SEM images of samples with varied roughness, the left one has lower R_Z (R_Z means peak to valley height) than the right one.

Samples C and D have almost identical structure heights but a 2:1 peak-to-peak density ratio. These samples allowed us to test how peak-to-peak density affected wetting properties of a stamped PC surface. The only difference between the processing parameters used to make these two samples was a change in shot number. SEM images of the samples created to test the influence of peak-to-peak distance are shown in Figure

5.19. Mounds density (quantity of mounds in same area) was determined using LSCM.

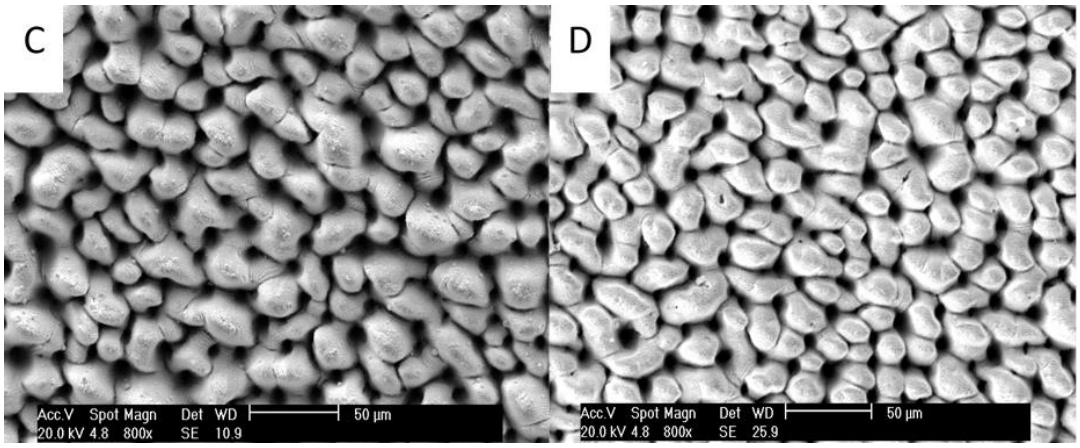

Figure 5.19. SEM images of samples with varied roughness. The image on the left has lower R_Z (R_Z means peak to valley height) than the sample on the right.

Stamps E and F have different structure types. Sample E has a high roughness but low structure height. Sample F has a lower roughness but a significantly higher structure height. Both fluence and shot number were varied to produce these samples.

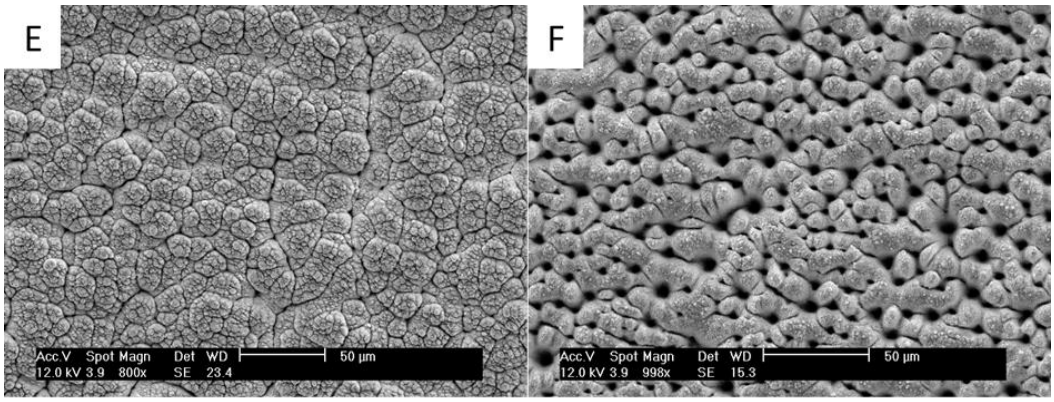

Figure 5.20. SEM images of samples made with varied mounds density (quantity of mounds in same area)

5.5.1 Different stamp roughness R_z

The two FLSP stamps used in this process have similar types of surface structures but differ in their average peak-to-valley height R_z, with the difference of 10 µm. Figure

21 shows the morphology of two imprinted PC surfaces stamped from FLSP stamps, the one imprinted from stamp A ($R_Z = 18$ μm) had a roughness $R_Z = 12 \pm 5\mu m, and$ the one imprinted from stamp B ($R_Z = 28$ μm) had a roughness $R_Z = 20 \pm 7\mu m$; the difference of R_z was consistent with their dies. The imprinted PC from stamp B had the higher contact angle than that of stamp A, correlating with the peak-to-valley height R_z.

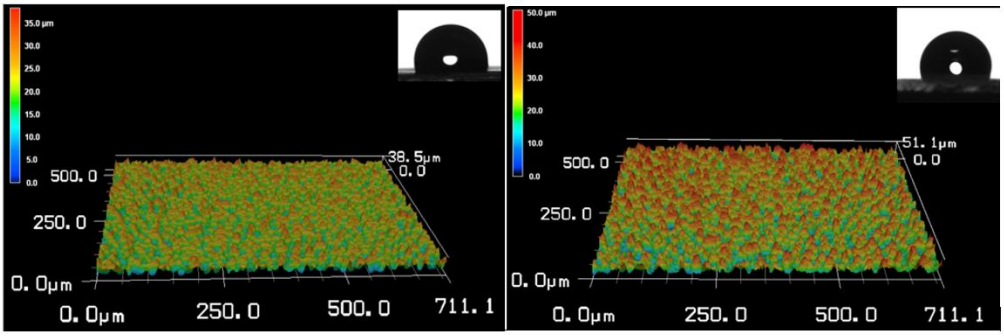

Figure 5.21. Surface structures obtained from laser confocal microscope, two imprinted from tungsten carbide samples A, B with different R_z.

5.5.2 Different stamp peak-to-peak distances

Two FLSP stamps used in this process had identical peak-to-valley distances $R_z\ of\ 20\mu m$, but the peak-to-peak distance are 40μm and 20μm, respectively, this peak-to-peak distance ratio between surface C and D was 2:1. Figure 5.22 shows the morphology of two imprinted PC surfaces stamped from FLSP stamps, the one imprinted from stamp C (20 $(10)^{-4}$ mounds/ μm^2) had (10 $(10)^{-4}$ mounds/ μm^2), while the one imprinted from stamp D (10 $(10)^{-4}$ mounds/ μm^2) had 20 $(10)^{-4}$ mounds/ μm^2; the difference of peak-to-peak distance, or mound concentration is

inverse with their dies. The imprinted PC from stamp C had a higher contact angle than the one from stamp D. Both imprinted PCs changed the wetting behavior from the original flat PC surface, as shown from figure 5.22, PC sample from C has contact angle of 108.5°, while the one from D is 70.8°. The results show that the one from stamp C with larger peak-to-peak distance was more hydrophobic; for the one from stamp D with smaller peak-to-peak distance was more hydrophilic.

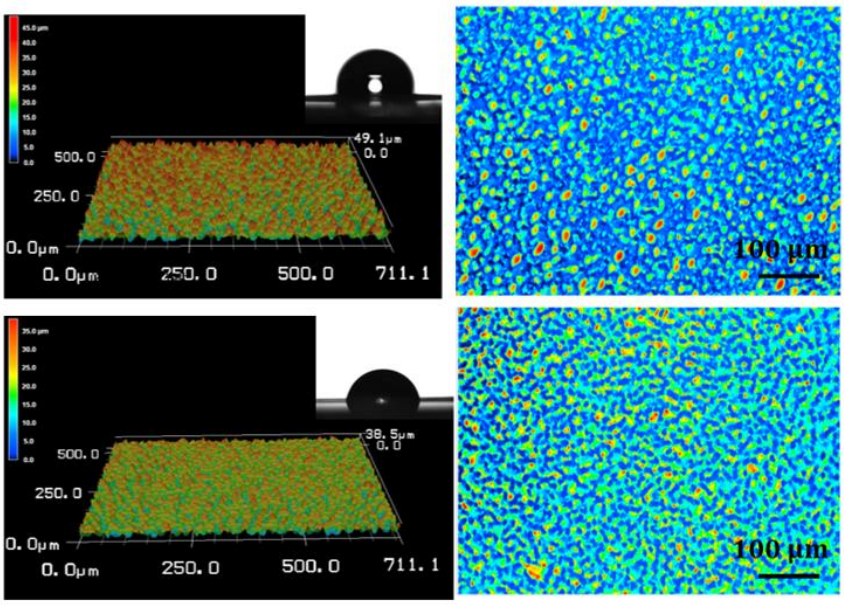

Figure 5.22. 3D images from laser confocal microscope, two imprinted from tungsten carbide samples C, D with different peak-to-peak distance; right: stamp C, D's mound concentration

5.5.3 Different surface structure patterns

Sample E and F were made with different types of surface morphology. Sample E has features with height variation, while the sample F surface did not have as much height variation but more nanostructure on the top of the microstructure. The imprinting results of samples E and F are shown in Figure 5.23. The difference of these two surfaces is obvious. First of all, the surface structure was different. For the one from sample F, the

surface had many shallow mounds corresponding with the low roughness of sample, the imprint from sample E had a higher peak and lower valley structure from the observation; thus, the peak-to-valley height, R_z, was different. However, the contact angle did not show a significant difference with each other or the flat surface. Contact angles are $64.1°$ and $67.2°$, respectively.

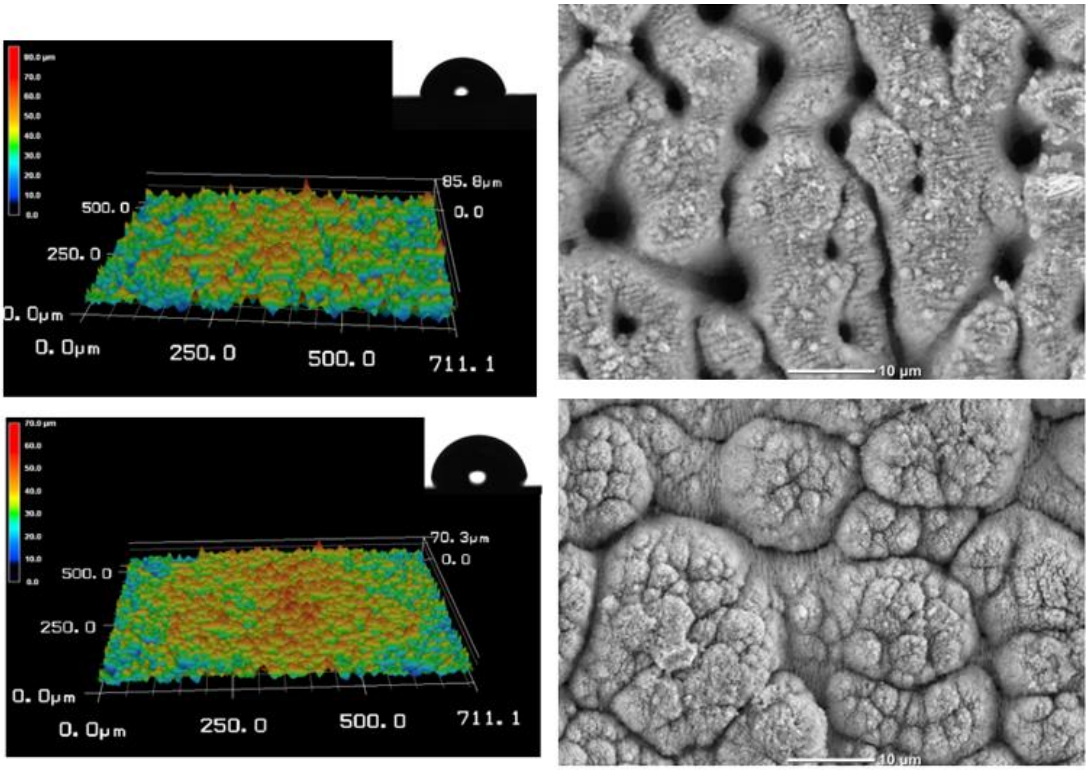

Figure 5.23. 3D images from LSCM. Two imprinted from tungsten carbide samples E, F with different surface structure types; right: SEM images of sample E, F with different surface structures.

Chapter 6. Duplicating FLSP surface structure by casting

Besides stamping FLSP surface structures on the blank materials, other methods were also explored to duplicate the FLSP mounds to other materials. Casting is a technique that is widely used in industry fields [81-84], it has the advantage of flexibility. This chapter describes duplicating FLSP surface structures by casting. PDMS (Polydimethylsiloxane) and PU (Polyurethane) were synthesized to cast the FLSP surface structure.

6.1 Experiment protocol for casting FLSP surface

An FLSP tungsten carbide surface was used as the casting mold; the surface structure of FLSP die is shown in Figure 6.3. The casting liquid applied was Dow Corning Sylgard 184 silicone elastomer, one of the most commonly used casting solutions. It is composed of two components. The final product is often used as a protective coating for LED lighting, power supplies, transformers, sensors, amplifiers, and connectors [85-89].

The facility that was used for the casting process is showed Figure 6.1. An FLSP WC mold was glued to a glass dish by carbide tape. Then part A and part B PDMS components was mixed in a 10:1 weight ratio, and the mixture of the two components were poured into the glass dish with the FLSP WC mold. After more than 24 hours, the solidified PDMS is carefully demolded, forming the negative FLSP surface on the

PDMS.

Figure 6.1. Part A and B of Dow Corning Sylgard 184 silicone elastomer (left) and the FLSP WC mold (right).

After producing the PDMS sample with negative FLSP surface structure on its surface, another experiment was to use the negative PDMS surface as the casting mold to produce a positive of original FLSP surface. Since PDMS is a relatively soft material, the casting solution for the second casting was PU. As in the above method, part A and part B components of PU were mixed in a 1:1 weight ratio, and the mixture was poured into the PDMS mold.

Since the PU's curing time is much less, so the above-mentioned process could be completed within an hour. After two hours, the PU sample was fully cured.

Figure 6.2. Part A and B of Environ Molds PU casting resins

6.2 Results of casting

The results of casting PDMS and PU surface structures are shown in this section. The wetting behavior of the PDMS surface was also measured by droplet testing.

6.2.1 Negative surface

PDMS is one of the most common material used for casting [90], and the casted surface morphology is shown in the Figure 6.3(b), while Figure 6.3(a) shows the FLSP die morphology. The average peak-to-valley height of the FLSP tungsten carbide sample was 110 μm. The average peak-to-valley height of the PDMS surface was 67.4 μm, which is more than half that of the FLSP surface. Unlike the cold-stamped FLSP surface shown in chapter 5, and although the casting was done in open air at room temperature, the PDMS sample surface showed an obvious mound-like structure with round peaks. These round peaks were formed from the valley of the FLSP WC surface, the repeated mounds were relatively even with each other. Furthermore, the contact angle of the PDMS was also increased for 104 degrees from the flat surface to 142 degrees.

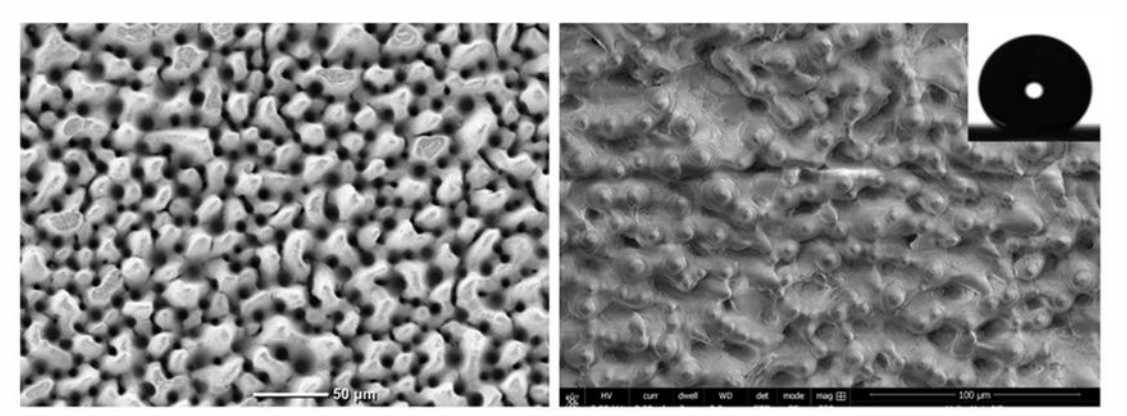

(a) (b)

Figure 6.3. SEM images of FLSP tungsten carbide surface(a) and the casting PDMS(b)

Another is contact angle, Figure 6.4 shows the record of contact variation. The flat reference PDMS surface was measured on the same PDMS sample regions which is not casted from FLSP WC, so the composition was exactly the same with the negative FLSP regions as well as the process environments. On one hand, it was clear that patterned negative FLSP surface morphology could improve PDMS's surface wetting behavior. The average contact angle increased from 104 degrees to 142 degrees. On the other hand, it was observed that after three weeks, the negative PDMS sample became more hydrophobic with a contact angle larger than 150 degrees.

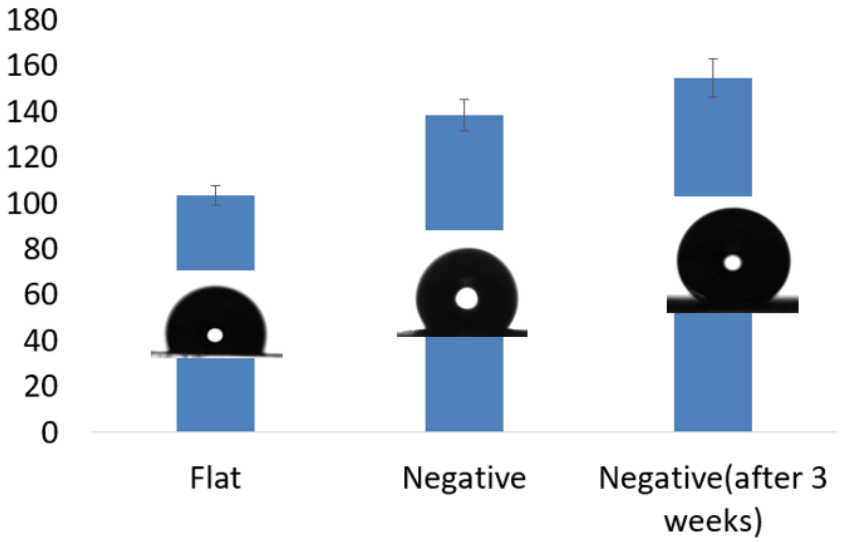

Figure 6.4 Contact angle variation of different PDMS sample

6.2.2 Positive surface

The results of the second casting of the PU sample are shown in Figure 6.5. Comparing the peak-to-valley height of the PDMS surface which is the casting mold of the PU sample, the PU surface completely replicated the negative PDMS surface with a peak-to-valley height of 74.2 μm.

What's more interesting, PU is a material harder than PDMS. The hardness of PU is higher than PDMS, so it can be used for more applications. In industry, the PU is used as hard-plastic parts [90-93]. The cast PU surface showed similar "negative" surface with the FLSP surface with peaks.

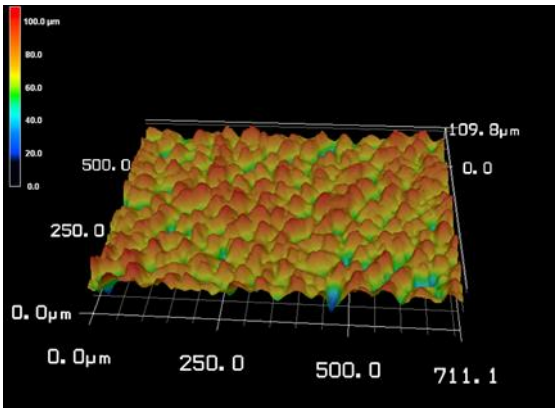

Figure 6.5. Lase confocal microscope scanning image of positive PU surface

6.2.3 Comparison of the FLSP mold and cast surface

Figure 6.6 shows the laser confocal microscope scanning of three kinds of surfaces from casting experiments. From the three morphologies of the three surfaces, the positive PU surface was similar to the FLSP WC surface in height and peak-to-peak distance. It makes sense that the PU surface had the same peak-to-peak distance with the FLSP surface, because for the negative surface, the peak-to-peak distance is the valley to valley distance in the FLSP WC sample. After the second casting, the peak-to-peak distance was duplicated again to the positive PU surface. The peak-to-peak distance was a parameter that reflects the mound concentration. Compared with the PU surface, the negative PDMS surface showed “negative” surface to the FLSP WC molds.

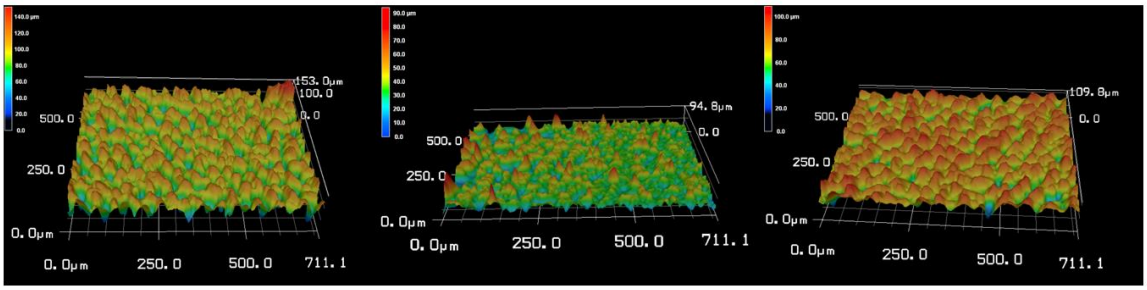

Figure 6.6. Comparison between FLSP tungsten carbide, PDMS and PU surface (from left to

right)

After casting, the average R_Z of PDMS and PU are 67.8 µm and 74.2 µm, respectively, while the FLSP surface has an average R_Z of 113 µm. Comparing the peak-to-valley roughness of FLSP WC, PDMS, and PU, it was clear that both the cast PDMS and PU surfaces were shorter than FLSP WC from peak-to-valley height R_Z, and nearly half that of the FLSP mounds. But the differences between PDMS and PU were much smaller. The comparison figure shown in Figure 6.7 indicating that the PDMS did not completely replicate the FLSP WC surface structure because the poured liquid PDMS solution did not fill the deep crevices of the FLSP WC mound valleys because air was trapped between the narrow valley of the mounds which could not be displaced. However, the PU solution completely replicated the PDMS surface structure with a similar average R_Z. The first casting PDMS surface was different with the second casting PU surface according to the surface roughness. The smaller size of FLSP surface valley and the air between the valleys contributed to such difference.

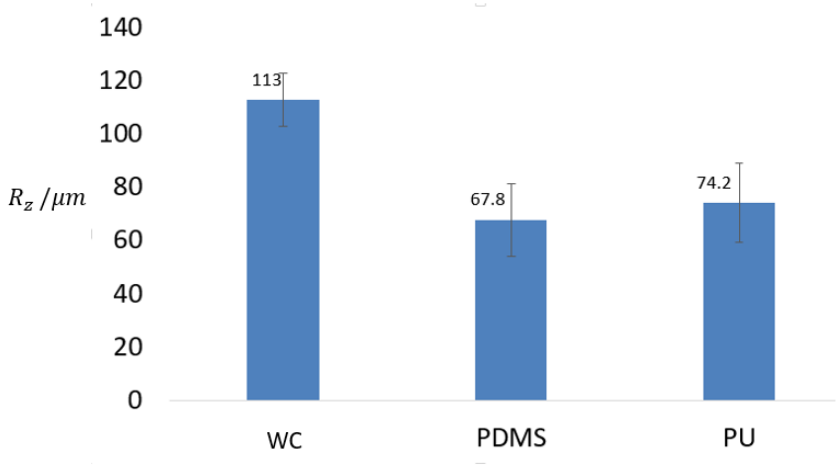

Figure 6.7. Peak-to-valley roughness comparison between FLSP WC, PDMS and PU samples

6.3 Conclusion

Casting experiments were designed to evaluate if this method is feasible for duplicating FLSP surfaces. Castings were done to produce negative and then positive surfaces.

After casting, it was noted that although the negative PDMS surface peak-to-valley roughness was only half of the FLSP WC mound, but the patterned surface structure greatly changed the PDMS wetting behavior, becoming it much more hydrophobic. This improvement was even greater after three weeks. The hydrophobic surface became superhydrophobic with a contact angle larger than 150 degree. This “Hydrophobic recovery” due to the migration of free siloxanes from the bulk to the surface.

Another discovery in this casting study is although the first casting did not completely duplicate the FLSP WC surface due to incomplete filling trapped air at the narrow valley bottom, the second casting could completely duplicate the negative PDMS surface structure. If attempting to produce large a scale positive FLSP surface, casting is a good method to apply. The casting quality depends on the first casting.

Chapter 7. Anti-icing property test of different imprinted FLSP surfaces

A material's good anti-icing performance is desired in many applications, ice and wet-snow adhesion and excessive accumulation will cause serious problems in high altitude and cold-climate regions. Furthermore, the widely applied LED lights causing no heat to melt surface ice comparing with the traditional bulbs. It made the anti-icing requirements of the signal surface more significant. Micro/nanostructured surfaces such as the lotus-leaf-like structure also have excellent anti-icing or icephobic properties [96-98]. This chapter presents the anti-icing property test of the imprinted FLSP sample surface produced from chapter 4. Some FLSP surface anti-icing test results will be presented as well.

7.1 Introduction of ice formation

Ice nucleation occurs when the temperature cools below water's freezing point. Nucleation occurs at impurities in water from mechanical shock, thermal fluctuation, or contact with a cooled surface. Since the nucleation barrier is a function of surface wettability, the heterogeneous critical energy barrier of a super hydrophobic surface approaches the homogeneous critical energy barrier.

Nucleation initiates at the liquid-vapor interface under a sufficient shearing gas flow or solid-liquid interface when heterogeneous critical activation energy is lower. When it is initiated, freezing occurs. Droplet freezing is in two phases. Firstly, the temperature of the droplet increases to thermodynamic equilibrium within milliseconds. Ice

dendrites propagate throughout the volume of the droplet originating from the nucleation site [103]. The second phase is slower than the first phase, the remaining part in the droplet freezes [104].

In the natural world, the first step of ice formation is attaching water to the surfaces, driving icy-snowy weather or from condensation. Then, the rapidly cool temperature freezes the water to ice.

7.2 Influence of surface wetting property

Surfaces with superhydrophobic properties also have anti-icing behavior[105-109]. Surfaces with different wettability often have a micro/nanostructure. According to the work of Guo et al., this micro/nanostructure also has a robust anti-icing behavior[110]. If ordering the anti-icing property of different surface structures from strong to weak, they are micro/nanostructured surface, nanostructured surface, microstructured surface and smooth surface [110]. This order is also consistent with the order of their wetting behavior.

7.3 Experimental methods and materials

Materials used for the anti-icing test were FLSP Al samples, FLSP PC samples and imprinted PC samples. FLSP PC and imprinted PC samples were described in chapter 5.

This anti-icing test can be divided into a condensation test and a freezing test. The condensation test was conducted in by the cooling system shown in Figure 7.1. The

temperature was set just below 0℃. Samples were placed on the holder (shown on the right of Figure 7.1) which could be moved under the optical microscope for observation of the actual freezing processes in real time.

Figure 7.1. Litron thermal system for condensation freezing. Left: control system, right: sample holder

When outdoor icing conditions arose on the University of Nebraska-Lincoln Campus, this study took advantage of the weather opportunity. A rain-ice-snow storm was forecast for January 11th, 2018. A simple apparatus shown in Figure 7.2 was made to hold the PC samples off the ground at 45 degrees facing the direction of the wind during the storm. The samples were exposed to the ice storm for three hours on the north side of the Walter Scott Engineering Center and Nebraska Hall (where the lab located).

Figure 7.2. Image of apparatus used to place PC samples in outdoor icing conditions.

7.4 Experimental results & discussion

The condensation for the unprocessed PC and imprinted PC is shown in Figure 7.3. When the sample was placed on the holder, heat transferred rapidly, because of the temperature difference between the sample and environment. The water vapor in the environment condensed on the sample surface. So, for the unprocessed surface which was flat and smooth, it was easy to observe that water drops formed on the surface. At the beginning, the water drops were small. As the number of water droplets increased, agglomeration occurred. The imprinted PC with a structured surface appeared to resist condensation, as no condensed droplets were observed.

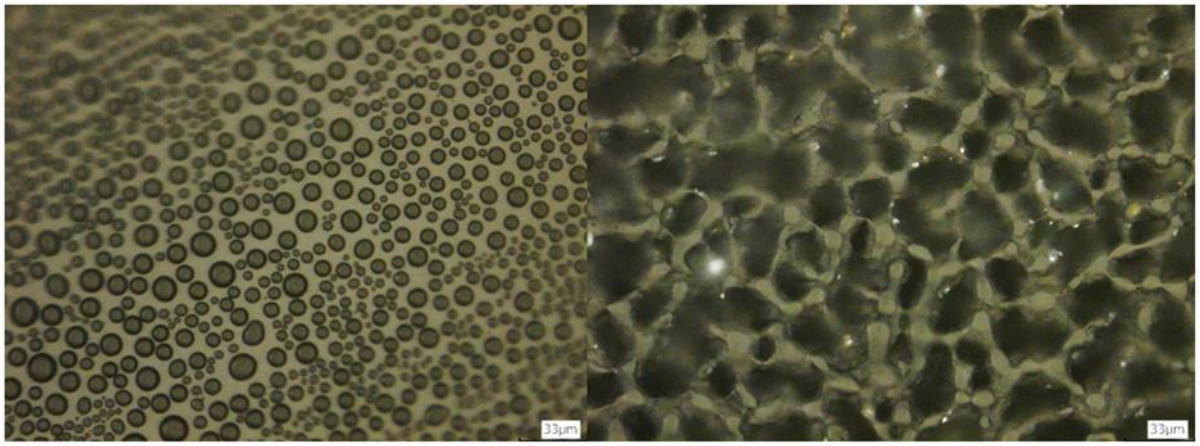

Figure 7.3. Condensation comparison between unprocessed PC on the left and imprinted PC surface on the right.

As a reference, an unprocessed Al and an FLSP Al were used for the outdoor test to examine their surface anti-icing behavior. Figure 7.4 shows the icing behavior on both samples. There were many ice flakes on the unprocessed Al surface, while the FLSP Al resisted ice formation and build-up completely. It indicated that the unprocessed Al attached to many water drops during the rainy weather. After the temperature decreased, the water spread on the Al surface, freezing to ice, As the temperature increased the ice structure broke down from inside, resolving in many small ice flakes. Under the same conditions, water drops from the rain could not stay on the surface of the superhydrophobic FLSP Al. So, when the temperature decreased, there was no ice formed on the FLSP Al surface.

Figure 7.4. Condensation comparison between unprocessed Al on the left and imprinted Al surface on the right.

One imprinted PC, one FLSP PC and one unprocessed PC sample were also tested outdoors. Among the three samples, FLSP PC had the most hydrophobic surface ($CA = 148°$), and the unprocessed PC had the worst wetting behavior($CA = 98°$) (but it was still a hydrophobic surface). After being outdoors for more than twenty hours, these PC samples experienced rainy and snowy weather. From the results from Figure 7.4, like the unprocessed Al surface shown above, the unprocessed PC surface was covered with large ice flakes, but only weakly adhered to the surface. The FLSP PC surface was covered by a few ice balls; these were also weakly adhered. The imprinted PC surface also had ice formation, but the coverage was less than that of the unprocessed PC surface. After the snow, all samples were covered by layers of snow, but removal was easy.

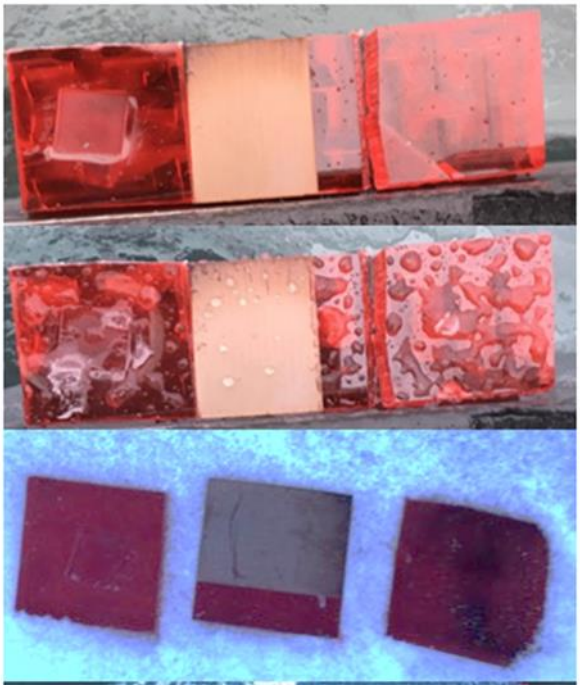

Figure 7.5. Outdoor icing test during the January 11th, 2018 ice storm; from left to right: Imprinted PC, FLSP PC, unprocessed PC

Other results of the outdoor icing experiment of imprinted PC, FLSP PC, and unprocessed PC are shown in Figure 7.5. They were consistent with the results shown in Figure 7.4, as FLSP PC had the least ice present on the surface. The situation of imprinted PC varied by imprint quality. The peak-to-valley roughness decreased from A to B to C as did the CA.

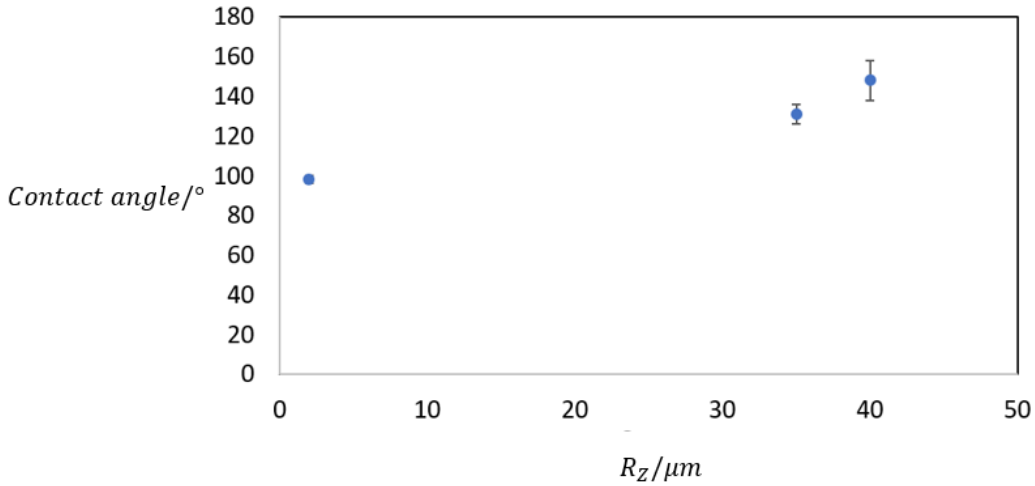

Figure 7.6. Contact angles variation by surface roughness

The ice region areas were also consistent with this order.

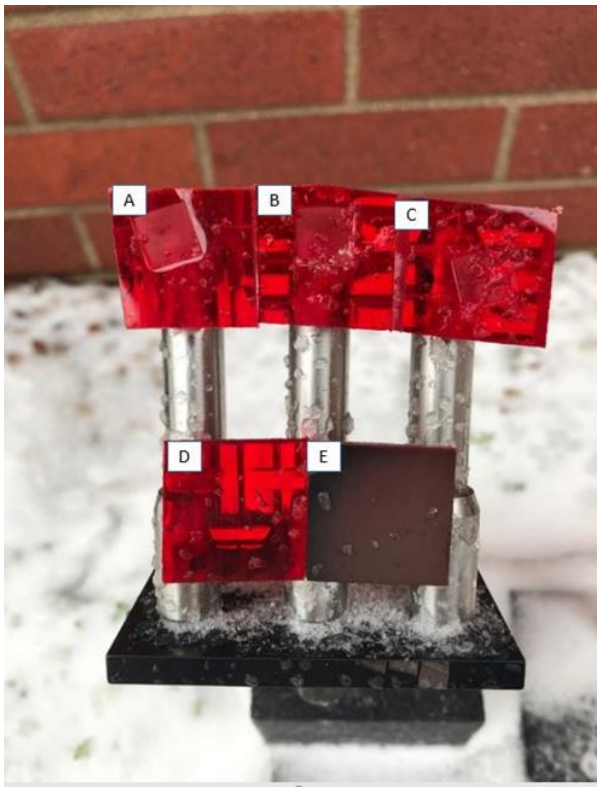

Figure 7.6. Top row A-C are specimens with stamped regions as marked. Specimen D is unprocessed. Specimen E is FLSP

Chapter 8. FLSP die's strength as the stamp

During the imprint process of the FLSP surface structure, the die is subjected to a pressure to imprint the micro/nano-structure on the blank materials. So, the FLSP die's material strength, in particular, the micro or nano scale mound's strength is very important, because it determines if the stamps can be applied multiple times. This chapter focus on the FLSP surface morphology change before and after stamping.

8.1 Experiment setup for observing before and after FLSP stamp surface

There were two materials used as FLSP surface die in this study, Ti an WC. Firstly, the before and after morphology was observed by scanning electron microscope for an over-all image, then focused on each mound by Keyence Laser confocal scanning microscope.

To observe the surface morphology's change before and after stamping, it is critical to accurately fix the sample's position under the microscope. A microscale cross mark made by laser ablation was made on each sample as the reference sign to mark the position of the surface structure. What is more, since the FLSP sample was $1 \times 1\ cm^2$, which was much larger the observation scale, the position on the microscope stage should also be the same before and after stamping. Thus, a custom-made aluminum panel with grids and a pair of clips shown in Figure 8.1 was applied to fix the position of the sample.

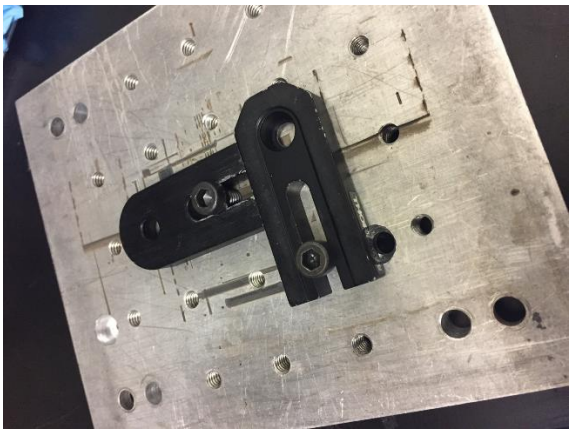

Figure 8.1. Custom-made panel to fix the sample's position on Keyence laser confocal scanning microscope.

8.2 Results of before and after stamping

8.2.1 FLSP Ti surface

The FLSP Ti surface was selected as a die due to it strong mechanical property. The die and blank material for this stamping were FLSP Ti and oxygen-free cooper (OFC), respectively. The applied force was 1 ton at room temperature. Figure 8.2 shows FLSP surface between before and after stamping. Before stamping, it has a typical peak-valley surface structure with a nanoparticle covering; stamping caused a significant change in the surface structure. The peak tops appear fractured. The FLSP Ti mounds were not strong enough as the die in the stamping process.

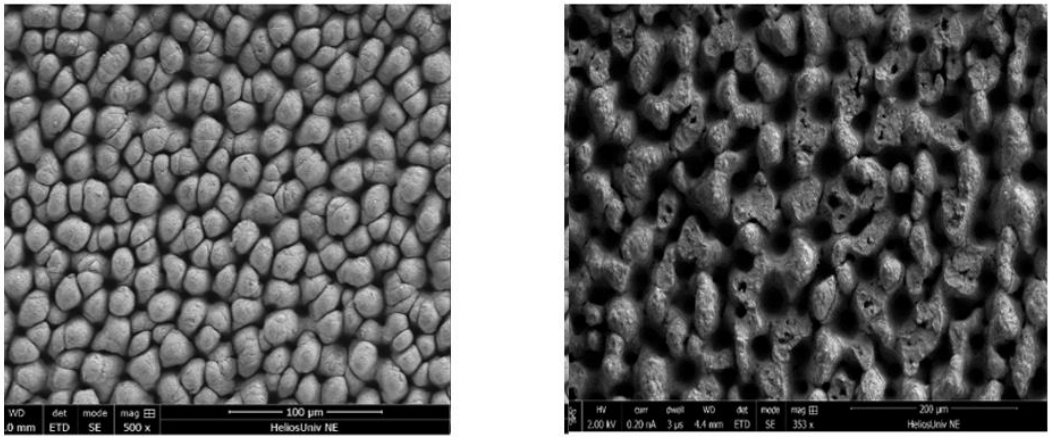

(a) (b)

Figure 8.2. SEM image of before (a) and after stamping FLSP Ti surface (b).

8.2.2 FLSP WC surface

FLSP WC was another material used as the die. In this experiment, FLSP WC and OFC were used as die and blank, respectively. The load used on them was 1 ton, and stamping was conducted at room temperature. Figure 8.3 shows the surface structure before and after stamping. Figure 8.3 (a)shows the surface morphology of FLSP WC. It shows to a typical peak-to-valley FLSP structure, but the mound concentration is not as high as the FLSP Ti surface. Figure 8.3 (b) shows the surface morphology after stamping. The mound shape is similar before and after stamping. The white regions were caused by the compression of the nanoparticle covered layer during stamping.

Compared with FLSP Ti, WC performed better as a die during stamping.

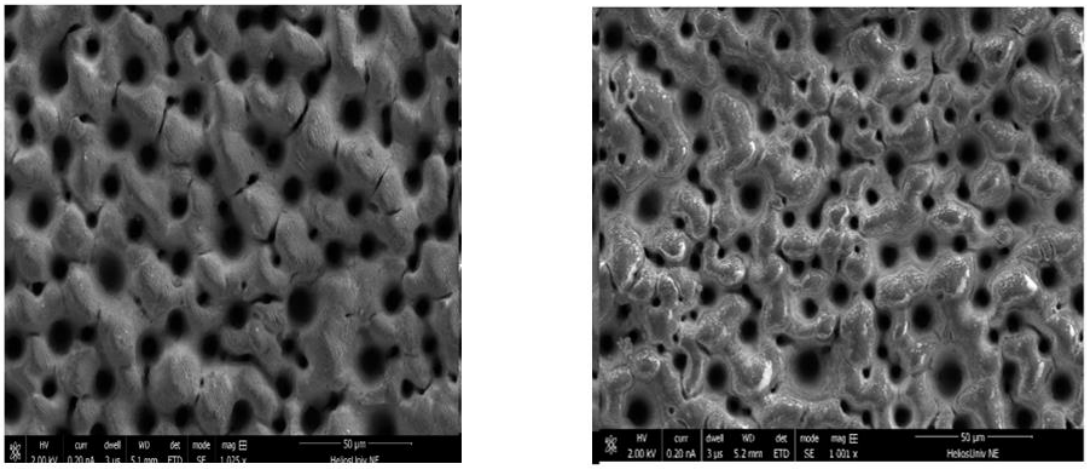

(a) (b)

Figure 8.3. SEM image of before (a) and after stamping FLSP WC surface (b).

The FLSP WC surface morphology change before and after stamping by line scanning the same mound morphology is shown in Figure 8.3 and Figure 8.4. These experiments were conducted on several WC samples, two of them are shown in Figure 8.4 and Figure 8.5.

Both experiments were conducted after a load of 1 ton was applied, but the one from Figure 8.4 was processed at the temperature of 120 ℃. From the line scan of the same mound position, it was observed that although the morphology had a slight change, the basic shape of the mound had little variation. This also could be concluded from the overlay of two scanning lines with an average height difference of 3 μm.

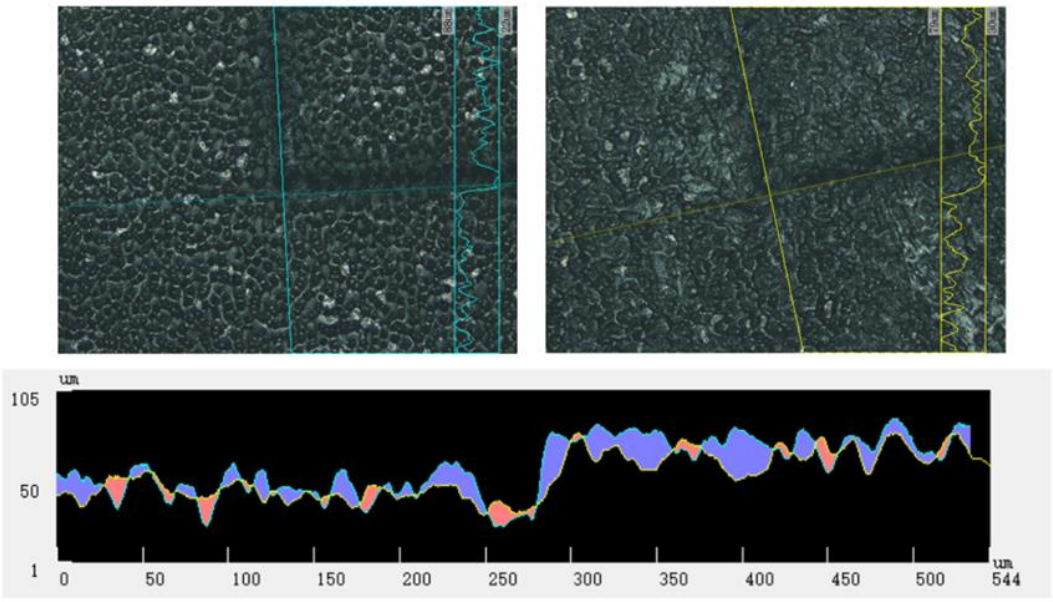

Figure 8.4. Two-line scans through the same portion of one WC die before (left) and after (right) stamping

The experiment in Figure 8.4 had the same stamping load of 1 ton, but applied at room temperature. The average height difference of before and after stamping of the mound was 3 μm.

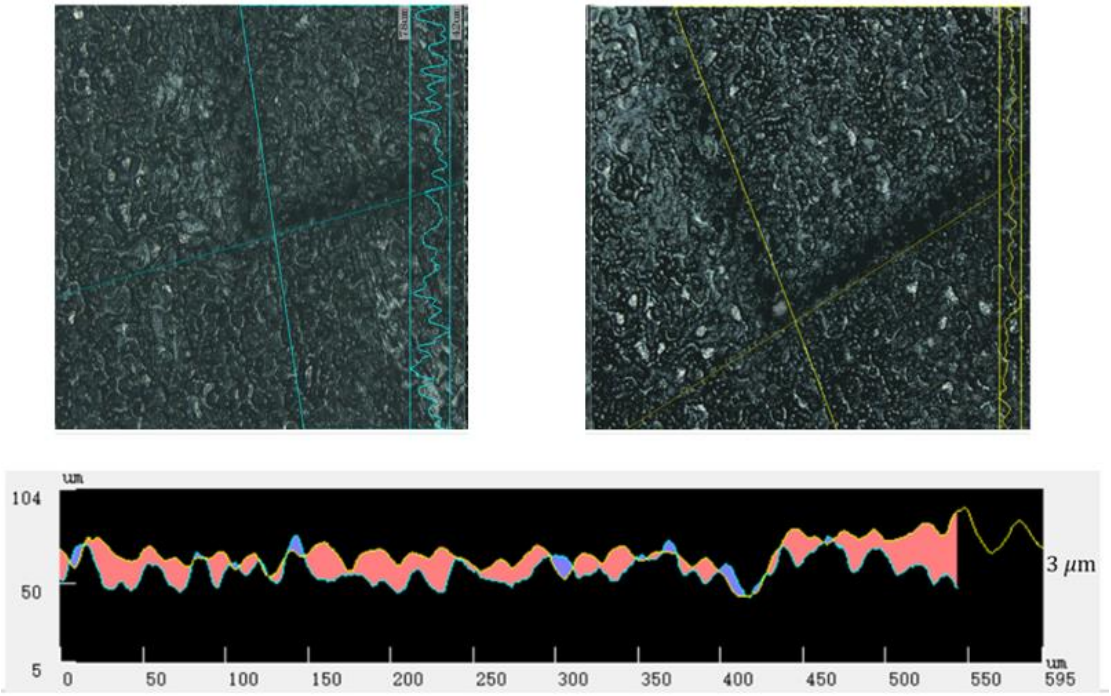

Figure 8.5. Two-line scans through the same portion of second WC die before (left) and after (right) stamping

The FLSP WC samples average peak-to-valley distance before and after stamping are recorded as shown in Figure 8.5. The stamping process for each sample was different. Sample 9 had the largest roughness difference before and after stamping: the roughness difference already reached 30 μm. It was because the stamping process was operated under large pressure (3 ton) and high temperature (200 ℃). For other FLSP WC samples, this value range was within 10 μm.

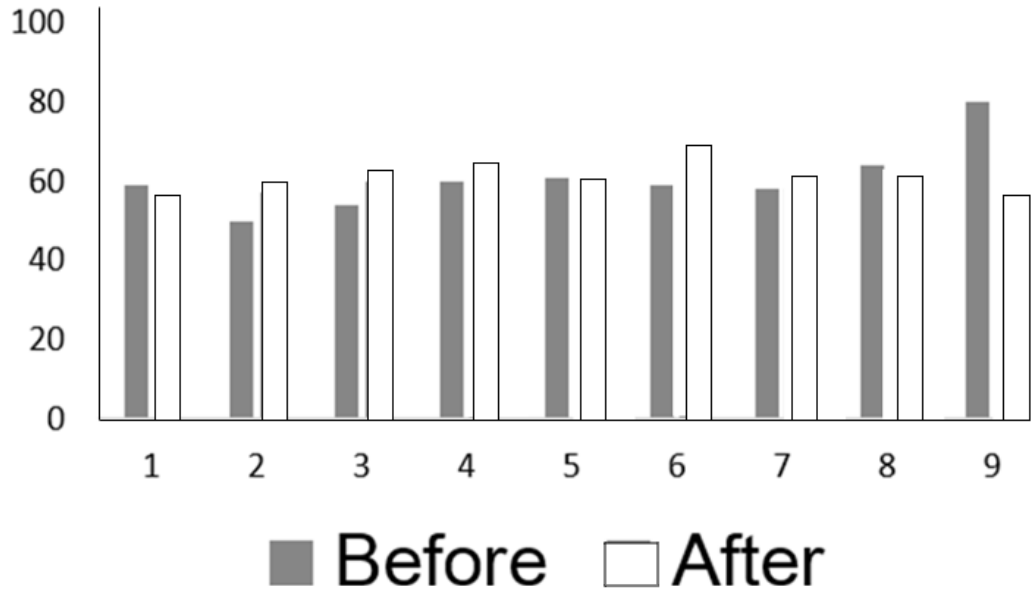

Figure 8.6. Average of nine FLSP WC peak-to-valley roughness before and after stamping

8.3 Conclusions

Two kinds of FLSP surfaces were used as FLSP WC die during stamping. By tracking the surface variation of the before and after surface structure, it was determined that FLSP WC has better performance in stamping than FLSP Ti. It could be applied for multiple stampings.

Chapter 9. Conclusions and future work

Femtosecond laser can produce different kinds of surface micro/nano-structures. This special surface structure introduced the change of some material properties, in particular, the wetting behavior. This study investigated different imprint methods duplicating the femtosecond laser induced surface structure, as well as its wetting property. A series of experiments was conducted, and from the results of these experiments the following conclusions can be made.

9.1 Conclusions

Based on the research performed in this study the following conclusions can be made:

1) Femtosecond laser processed railroad signal lens covers directly is a feasible way to make the railroad lens cover superhydrophobic. The direct laser process slightly alters the color of the lens, but does not alter the color when illuminated. The FLSP surfaces performed very well in an outdoor real life icing environment.

2) Stamping of FLSP surfaces into a heated railroad lens cover also was demonstrated to be able to affect the anti-icing properties of railroad lens. Furthermore, the stamping conditions influence the imprint quality and ultimately the wetting behavior:

i Temperature: 120 ℃ is an ideal temperature for stamping railroad signal lens, both lower and higher temperatures results in poor imprint quality, for lower temperature, only pit-like morphology developed; for higher temperature, it is easy to damage the PC samples since they stick to the stamps and can be deformed when separated;

ii Load: Even though one sets the stamp environment be 120 ℃ (optimum) larger applied loads is not helpful for duplicating the surface morphology (due to large elasticity).

3) Stamps' morphology also has large influence on the imprint quality:

i Roughness R_z : higher roughness results in higher imprinted surface roughness, and it can improve the surface hydrophobicity;

ii Peak-to-peak distance: the imprinted peak-to-peak distance is inverse with the stamp, for the PC materials, the higher peak-to-peak distance, the more hydrophilic it be;

iii Different surface structure types: different surface structure types result different surface morphology on the imprinted PC surface but has limited influence on the wetting property.

4) With casted surface structure from FLSP tungsten carbide, PDMS largely improved its hydrophobicity from hydrophobic to superhydrophobic without any modification.

5) No water drops formed on the imprinted surface when operating condensation test;

6) Both imprinted and FLSP railroad signal lens surface have promise for anti-icing railroad lens applications.

In summary, railroad signal lens polycarbonate (PC) became anti-icing for both directly writing FLSP surfaces on the lens or using a stamping process. Further research will be needed to determine the most economically method to actually use in a commercial application of the technology developed in this study.

9.2 Future work

This current work is based on a large number of experiments, and static computational modeling of the stamping process. There are some shortages during investigating and large potentials for exploring.

Firstly, the separation of the stamped samples is a problem to overcome. It is easy to damage the imprinted surface during separation. Application of lubricant will also affect the surface wetting property due to a surface chemistry change. Considering massive production, hot rolling may be an effective method for this problem.

Then, there is large potential to improve the imprint quality of polymers. The polymer is a soft material with a low melting temperature. Since casting has been proven to be an effective method to duplicate the surface morphology, most industries use casting as the shape forming method to produce plastic products with different geometries, an for

imprinting and combining with these shape forming methods to obtain a better wetting property.

Third, by studying different micro/nano-structures of the FLSP surface, it was discovered that the narrow space between mounds or the bottom of the valley structure, is hard to be imprinted. There is an air barrier for other materials to reach. It is highly related with the state of the blank materials and the pressure works on it to duplicate the surface structure in smaller scale. For stamping, the softer property of the blank can be created by heating, but the temperature is below its melting temperature; for casting, the state of the blank was initiated with liquid, but it could not flow to the narrow space due to the air barrier. For future imprint studies, this air barrier should be considered to overcome.

Finally, whether the nanostructure of the FLSP surface can be imprinted on other materials still is not discovered. There are large loads working on the FLSP surface during stamping, and the nanostructure of the FLSP surface is partly damaged from the before and after imprinting comparison. By improving the FLSP surface structure mechanical property, a more accurate negative surface can be produced in nanoscale.

References

[1] R. Leipold, M. Boese, and L. Fottner, “The Influence of Technical Surface Roughness Caused by Precision Forging on the Flow Around a Highly Loaded Compressor Cascade,” *J. Turbomach.*, vol. 122, no. 3, p. 416, 2000.

[2] R. P. Taylor, “Surface Roughness Measurements on Gas Turbine Blades,” *J. Turbomach.*, vol. 112, no. 2, p. 175, 1990.

[3] C. H. Jonda, B. R. Mayer, and U. Stolz, “Surface roughness effects and their influence on the degradation of organic light emitting devices,” *J. Mater. Sci.*, vol. 35, pp. 5645–5651, 2000.

[4] J. P. Bons, “A Review of Surface Roughness Effects in Gas Turbines,” *J. Turbomach.*, vol. 132, no. 2, p. 021004, 2010.

[5] E. Donnelly, S. P. Baker, A. L. Boskey, and M. C. H. Van Der Meulen, “Effects of surface roughness and maximum load on the mechanical properties of cancellous bone measured by nanoindentation,” *J. Biomed. Mater. Res. - Part A*, vol. 77, no. 2, pp. 426–435, 2006.

[6] U. Lohbauer, F. A. Müller, and A. Petschelt, “Influence of surface roughness on mechanical strength of resin composite versus glass ceramic materials,” *Dent. Mater.*, vol. 24, no. 2, pp. 250–256, 2008.

[7] Y. Jiang, B. Li, and Y. Tanabashi, “Estimating the relation between surface roughness and mechanical properties of rock joints,” *Int. J. Rock Mech. Min. Sci.*, vol. 43, no. 6, pp. 837–846, 2006.

[8] R. Seemann, M. Brinkmann, E. J. Kramer, F. F. Lange, and R. Lipowsky, “Wetting morphologies at microstructured surfaces,” *Proc. Natl. Acad. Sci.*, vol. 102, no. 6, pp. 1848–1852, 2005.

[9] Y. Y. Yan, N. Gao, and W. Barthlott, “Mimicking natural superhydrophobic surfaces and grasping the wetting process: A review on recent progress in preparing superhydrophobic surfaces,” *Adv. Colloid Interface Sci.*, vol. 169, no. 2, pp. 80–105, 2011.

[10] Rockett, A. Chapter 11. Physical vapor deposition, In The materials science of semiconductors, 1st edition; Springer, New York, 2008; pp 505-572.

[11] Mattox, D.M. Chapter 1. Introduction. In Handbook of physical vapor deposition (PVD) processing, 2nd edition; William Andrew, New York, 2010; pp 1-25.

[12] http://www.ajaint.com/what-is-sputtering.html

[13] http://www.emu.uct.ac.za/lecture-5-confocal-laser-scanning-microscopy

[14] D. C. Emmony, R. P. Howson, and L. J. Willis, “Laser mirror damage in germanium at 10.6 μm,” *Appl. Phys. Lett*., vol. 23, no. 11, pp. 598–600, 1973.

[15] S. A. Akhmanov, V. I. Emel’yanov, N. I. Koroteev, and V. N. Seminogov, “Interaction of powerful laser radiation with the surfaces of semiconductors and metals: nonlinear optical effects and nonlinear optical diagnostics,” *Uspekhi Fiz. Nauk*, vol. 147, no. 12, p. 675, 1985.

[16] J. E. Sipe, J. F. Young, J. S. Preston, and H. M. Van Driel, “Laser-induced periodic surface structure. I. Theory,” *Phys. Rev. B*, vol. 27, no. 2, pp. 1141–1154, 1983.

[17] E. Results and P. Models, “Spontaneous Periodic Surface Structures on,” *Phys. Rev. B*, vol. 26, no. 10, p. 5366, 1982.

[18] M. Birnbaum, “Semiconductor surface damage produced by Ruby lasers,” *J. Appl. Phys*., vol. 36, no. 11, pp. 3688–3689, 1965.

[19] T.Tajima, J.M.Dawson. "Laser Electron Accelerator," *Phys.Rev.Letter*. vol. 4, no. 4, pp. 267–270, 1979.

[20] C. Rulliere, Femtosecond laser pulses. 1998.

[21] S. E. Clark and D. C. Emmony, “Ultraviolet-laser-induced periodic surface structures,” *Phys. Rev. B*, vol. 40, no. 4, pp. 2031–2041, 1989.

[22] https://www.laserfocusworld.com/articles/2015/05/ultrafast-laser-market-the-battle-of-value-vs-cost.html.

[23] R. G. Abell and B. J. Vote, “Cost-effectiveness of femtosecond laser-assisted cataract surgery versus phacoemulsification cataract surgery,” *Ophthalmology*, vol. 121, no. 1, pp. 10–16, 2014.

[24] Z. Sun et al., “Graphene mode-locked ultrafast laser,” *ACS Nano*, vol. 4, no. 2, pp. 803–810, 2010.

[25] M. E. Fermann and I. Hartl, “Ultrafast fibre lasers,” *Nat. Photonics*, vol. 7, no. 11, pp. 868–874, 2013.

[26] K. Askar et al., “Self-assembled self-cleaning broadband anti-reflection coatings,” *Colloids Surfaces A Physicochem. Eng. Asp*., vol. 439, pp. 84–100, 2013

[27] C. a Zuhlke, T. P. Anderson, and D. R. Alexander, “Formation of multiscale surface structures on nickel via above surface growth and below surface growth mechanisms using femtosecond laser pulses,” *Opt. Express*, vol. 21, no. 7, pp. 8460–8473, 2013.

[28] T. H. Her, R. J. Finlay, C. Wu, S. Deliwala, and E. Mazur, “Microstructuring of silicon with femtosecond laser pulses,” *Appl. Phys. Lett*., vol. 73, no. 12, pp. 1673–1675, 1998.

[29] A. Y. Vorobyev and C. Guo, “Colorizing metals with femtosecond laser pulses,” *Appl. Phys. Lett.*, vol. 92, no. 4, pp. 1–4, 2008.

[30] P. Simon and J. Ihlemann, “Ablation of submicron structures on metals and semiconductors by femtosecond UV-laser pulses,” *Appl. Surf. Sci*., vol. 109–110, pp. 25–29, 1997.

[31] C. M. Kruse, “Heat Transfer Enhancement and Applications of Femtosecond Laser Processed Metallic Surfaces: magistrska naloga,” pp. 1–100, 2014.

[32] M. J. Sher, M. T. Winkler, and E. Mazur, “Pulsed-laser hyperdoping and surface texturing for photovoltaics,” *MRS Bull.,* vol. 36, no. 6, pp. 439–455, 2011.

[33] D. E. Packham, “Surface energy, surface topography and adhesion,” *Int. J. Adhes.*, vol. 23, no. 6, pp. 437–448, 2003.

[34] J. F. McBride, C. S. Simmons, and J. W. Cary, “Interfacial spreading effects on one-dimensional organic liquid imbibition in water-wetted porous media,” *J. Contam. Hydrol.*, vol. 11, no. 1, pp. 1–25, 1992.

[35] M. K. Bernett and W. A. Zisman, “Effect of adsorbed water on wetting properties of borosilicate glass, quartz, and sapphire,” *J. Colloid Interface Sci.*, vol. 29, no. 3, pp. 413–423, 1969.

[36] W. D. Harkins and A. Feldman, “Films. The spreading of liquids and the spreading coefficient,” *J. Am. Chem. Soc.*, vol. 44, no. 12, pp. 2665–2685, 1922.

[37] M. Quirynen and C. M. L. Bollen, “The influence of surface roughness and surface-free energy on supra- and subgingival plaque formation in man: A review of the literature,” *Journal of Clinical Periodontology*, vol. 22, no. 1. pp. 1–14, 1995.

[38] Y. Lee, S. H. Park, K. B. Kim, and J. K. Lee, “Fabrication of hierarchical structures on a polymer surface to mimic natural superhydrophobic surfaces,” *Adv. Mater.*, vol. 19, no. 17, pp. 2330–2335, 2007.

[39] A. Lafuma and D. Quéré, “Superhydrophobic states,” *Nat. Mater.*, vol. 2, no. 7, pp. 457–460, 2003.

[40] Y. L. E. E. R. Whitet, “On Deviations from,” pp. 390–398, 1976.

[41] W. Choi, A. Tuteja, J. M. Mabry, R. E. Cohen, and G. H. McKinley, “A modified Cassie-Baxter relationship to explain contact angle hysteresis and anisotropy on non-wetting textured surfaces,” *J. Colloid Interface Sci.*, vol. 339, no. 1, pp. 208–216, 2009.

[42] G. McHale, N. J. Shirtcliffe, and M. I. Newton, “Contact-angle hysteresis on super-hydrophobic surfaces,” *Langmuir*, vol. 20, no. 23, pp. 10146–10149, 2004.

[43] A. K. Sasmal et al., “Fabrication of superhydrophobic copper surface on various substrates for roll-off, self-cleaning, and water/oil separation,” *ACS Appl. Mater. Interfaces*, vol. 6, no. 24, pp. 22034–22043, 2014.

[44] B. Balu, V. Breedveld, and D. W. Hess, “Fabrication of ‘roll-off’ and ‘sticky’ superhydrophobic cellulose surfaces-via plasma processing,” *Langmuir*, vol. 24, no. 9, pp. 4785–4790, 2008.

[45] X. Deng, L. Mammen, H.-J. Butt, and D. Vollmer, “Candle Soot as a tmeplate for a transparent robust superampiphobic coating,” *Science.*, vol. 335, no. 6, p. 67, 2012.

[46] T. Verho, C. Bower, P. Andrew, S. Franssila, O. Ikkala, and R. H. A. Ras, “Mechanically Durable Superhydrophobic Surfaces,” *Adv. Mater.*, vol. 23, no. 5, pp. 673–678, 2011.

[47] T. Nishino, M. Meguro, K. Nakamae, M. Matsushita, and Y. Ueda, “The Lowest Surface Free Energy Based on −CF 3 Alignment,” *Langmuir*, vol. 15, no. 13, pp. 4321–4323, 1999.

[48] T. Mao, D. C. S. Kuhn, and H. Tran, “Spread and Rebound of Liquid Droplets upon Impact on Flat Surfaces,” *AIChE J.*, vol. 43, no. 9, pp. 2169–2179, 1997.

[49] J. Fukai 98, M. Tanaka, "Maximum spreading of liquid droplets colliding with flat surfaces.” *J Chem Eng of Japan*, vol. 31, no. 3, pp. 456-461, 1998 .

[50] D. C. Vadillo, A. Soucemarianadin, C. Delattre, and D. C. D. Roux, “Dynamic contact angle effects onto the maximum drop impact spreading on solid surfaces,” *Phys. Fluids*, vol. 21, no. 12, pp. 1–8, 2009.

[51] E. Bormashenko, Y. Bormashenko, T. Stein, G. Whyman, and E. Bormashenko, “Why do pigeon feathers repel water? Hydrophobicity of pennae, Cassie-Baxter wetting hypothesis and Cassie-Wenzel capillarity-induced wetting transition,” *J. Colloid Interface Sci.*, vol. 311, no. 1, pp. 212–216, 2007.

[52] G. Whyman, E. Bormashenko, and T. Stein, “The rigorous derivation of Young, Cassie-Baxter and Wenzel equations and the analysis of the contact angle hysteresis

phenomenon," *Chem. Phys. Lett.*, vol. 450, no. 4–6, pp. 355–359, 2008.

[53] T. Koishi, K. Yasuoka, S. Fujikawa, T. Ebisuzaki, and X. C. Zeng, "Coexistence and transition between Cassie and Wenzel state on pillared hydrophobic surface," *Proc. Natl. Acad. Sci.,* vol. 106, no. 21, pp. 8435–8440, 2009.

[54] E. Bormashenko, "Why does the Cassie-Baxter equation apply?," *Colloids Surfaces A Physicochem. Eng. Asp.*, vol. 324, no. 1–3, pp. 47–50, 2008.

[55] D. Lacalle, A. Lamikiz, J. A. Sa, and L. N. Lo, "Improving the surface finish in high speed milling of stamping dies," vol. 123, pp. 292–302, 2002.

[56] M. Naderi, V. Uthaisangsuk, U. Prahl, and W. Bleck, "A Numerical and Experimental Investigation into Hot Stamping of Boron Alloyed Heat Treated Steels," pp. 77–84, 2008.

[57] J. Cao, B. L. Kinsey, H. Yao, V. Viswanathan, and N. Song, "Next generation stamping dies controllability and exibility," vol. 17, pp. 49–56, 2001.

[58] L. Peng, P. Hu, X. Lai, D. Mei, and J. Ni, "Investigation of micro/meso sheet soft punch stamping process and simulation and experiments," *Mater. Des.*, vol. 30, no. 3, pp. 783–790, 2009.

[59] U. Engel and R. Eckstein, "Microforming from basic research to its realization," vol. 126, no. January, pp. 35–44, 2002.

[60] S. Swaddiwudhipong, J. Hua, K. K. Tho, and Z. S. Liu, "Equivalency of Berkovich and conical load-indentation curves," *Model. Simul. Mater. Sci. Eng.*, vol. 14, no. 1, pp. 71–82, 2006.

[61] L. Min, C. Wei-min, L. Nai-gang, and W. Ling-Dong, "A numerical study of indentation using indenters of different geometry," *J. Mater. Res.*, vol. 19, no. 1, pp. 73–78, 2004.

[62] N. A. Sakharova, J. V. Fernandes, J. M. Antunes, and M. C. Oliveira, "Comparison between Berkovich, Vickers and conical indentation tests: A three-dimensional numerical simulation study," *Int. J. Solids Struct.*, vol. 46, no. 5, pp. 1095–1104, 2009.

[63] Z. H. Xu and X. Li, "Effects of indenter geometry and material properties on the correction factor of Sneddon's relationship for nanoindentation of elastic and elastic-plastic materials," *Acta Mater.*, vol. 56, no. 6, pp. 1399–1405, 2008.

[64] S. W. Moore, M. T. Manzari, and Y.-L. Shen, "Nanoindentation in elastoplastic materials: insights from numerical simulations," *Int. J. Smart Nano Mater.*, vol. 1, no. 2, pp. 95–114, 2010.

[65] A. Tibaldi, “Morphology of pyroclastic cones and tectonics are Joffe and Gaff unkel height of cone,” vol. 100, no. Table 1, 1995.

[66] J. X. Wei, K. M. Liew, and X. Q. He, “Mechanical properties of carbon nanocones,” *Appl. Phys. Lett.*, vol. 91, no. 26, pp. 1–4, 2007.

[67] Y. Wu, G. Wang, F. Wu, and Z. Hu, “Euclidean reconstruction of a circular truncated cone only from its uncalibrated contours,” *Image Vis. Comput.*, vol. 24, no. 8, pp. 810–818, 2006.

[68] A. Y. Vorobyev and C. Guo, “Direct femtosecond laser surface nano/microstructuring and its applications,” *Laser Photonics Rev.*, vol. 7, no. 3, pp. 385–407, 2013.

[69] Y. Song *et al.*, “Effect of topology and material properties on the imprint quality of the femtosecond-laser-induced surface structures,” *J. Mater. Sci.*, 2017.

[70] Z. Z. Fang, X. Wang, T. Ryu, K. S. Hwang, and H. Y. Sohn, “Synthesis, sintering, and mechanical properties of nanocrystalline cemented tungsten carbide - A review,” *Int. J. Refract. Met. Hard Mater.*, vol. 27, no. 2, pp. 288–299, 2009.

[71] R. . Rodríguez, J. . García, R. Sánchez, a Pérez, B. Garrido, and J. Morante, “Modification of surface mechanical properties of polycarbonate by ion implantation,” *Surf. Coatings Technol.*, vol. 158–159, pp. 636–642, 2002.

[72] J. M. Cariou, J. Dugas, L. Martin, and P. Michel, “Refractive-index variations with temperature of PMMA and polycarbonate.,” *Appl. Opt.*, vol. 25, no. 3, pp. 334–336, 1986.

[73] P. A. O’Connell and G. B. McKenna, “Large deformation response of polycarbonate: Time-temperature, time-aging time, and time-strain superposition,” *Polym. Eng. Sci.*, vol. 37, no. 9, pp. 1485–1495, 1997.

[74] R. A. W. Fraser and I. M. Ward, “Temperature dependence of craze shape and fracture in polycarbonate,” *Polymer (Guildf).*, vol. 19, no. 2, pp. 220–224, 1978.

[75] L. Zhu, Y. Feng, X. Ye, and Z. Zhou, “Tuning wettability and getting superhydrophobic surface by controlling surface roughness with well-designed microstructures,” *Sensors Actuators, A Phys.*, vol. 130–131, no. SPEC. ISS., pp. 595–600, 2006.

[76] K. J. Kubiak, M. C. T. Wilson, T. G. Mathia, and P. Carval, “Wettability versus roughness of engineering surfaces,” *Wear*, vol. 271, no. 3–4, pp. 523–528, 2011.

[77] L. Ponsonnet *et al.*, “Relationship between surface properties (roughness, wettability) of titanium and titanium alloys and cell behaviour,” *Mater. Sci. Eng. C*, vol. 23, no. 4,

pp. 551–560, 2003.

[78] J. I. Rosales-Leal *et al.*, “Effect of roughness, wettability and morphology of engineered titanium surfaces on osteoblast-like cell adhesion,” *Colloids Surfaces A Physicochem. Eng. Asp.*, vol. 365, no. 1–3, pp. 222–229, 2010.

[79] M. Lampin, R. Warocquier-Clérout, C. Legris, M. Degrange, and M. F. Sigot-Luizard, “Correlation between substratum roughness and wettability, cell adhesion, and cell migration,” *J. Biomed. Mater. Res.*, vol. 36, no. 1, pp. 99–108, 1997.

[80] Hideo Nakae, Ryuichi Inui, Yosuke Hirata, and Hiroyuki Saito, “Effects of surface roughness on wettability,” *Acta Mater.*, vol. 46, no. 7, pp. 2313–2318, 1998.

[81] J. S. Miller *et al.*, “Rapid casting of patterned vascular networks for perfusable engineered three-dimensional tissues,” *Nat. Mater.*, vol. 11, no. 9, pp. 768–774, 2012.

[82] A. Inoue and T. Zhang, “Fabrication of Bulk Glassy $Zr_{55}Al_{10}Ni_5Cu_{30}$ Alloy of 30 mm in Diameter by a Suction Casting Method,” *Materials Transactions, JIM*, vol. 37, no. 2. pp. 185–187, 1996.

[83] A. Inoue, T. Zhang, and T. Masumoto, “Production of amorphous cylinder and sheet of La55Al25Ni20 alloy by a metallic mold casting method,” *Materials Transactions, JIM*, vol. 31, no. 5. pp. 425–428, 1990.

[84] J. Hashim, L. Looney, and M. S. J. Hashmi, “Metal matrix composites: production by the stir casting method,” *J. Mater. Process. Technol.*, vol. 92–93, pp. 1–7, 1999.

[85] J. R. Anderson *et al.*, “Fabrication of topologically complex three-dimensional microfluidic systems in PDMS by rapid prototyping,” *Anal. Chem.*, vol. 72, no. 14, pp. 3158–3164, 2000.

[86] T. Fujii, “PDMS-based microfluidic devices for biomedical applications,” *Microelectron. Eng.*, vol. 61–62, pp. 907–914, 2002.

[87] and S. G. S. Bhattacharya, A. Datta, J. M. Berg, “Studies on Surface Wettability of Poly (Dimethyl) Siloxane (PDMS) and Glass Under Oxygen-Plasma,” *J.MicroElecMechSys*, vol. 14, no. 3, pp. 590–597, 2005.

[88] B. H. Jo, L. M. Van Lerberghe, K. M. Motsegood, and D. J. Beebe, “Three-dimensional micro-channel fabrication in polydimethylsiloxane (PDMS) elastomer,” *J. Microelectromechanical Syst.*, vol. 9, no. 1, pp. 76–81, 2000.

[89] M. W. Toepke and D. J. Beebe, “PDMS absorption of small molecules and consequences in microfluidic applications,” *Lab Chip*, vol. 6, no. 12, pp. 1484–1486,

2006.

[90] D. K. Chattopadhyay and K. V. S. N. Raju, “Structural engineering of polyurethane coatings for high performance applications,” *Prog. Polym. Sci.*, vol. 32, no. 3, pp. 352–418, 2007.

[91] W. M. Huang, B. Yang, L. An, C. Li, and Y. S. Chan, “Water-driven programmable polyurethane shape memory polymer: Demonstration and mechanism,” *Appl. Phys. Lett.*, vol. 86, no. 11, pp. 1–3, 2005.

[92] M. M. Demir, I. Yilgor, E. Yilgor, and B. Erman, “Electrospinning of polyurethane fi bers,” *Polymer (Guildf).*, vol. 43, no. 11, pp. 3303–3309, 2002.

[93] P. Jain and T. Pradeep, “Potential of silver nanoparticle-coated polyurethane foam as an antibacterial water filter,” *Biotechnol. Bioeng.*, vol. 90, no. 1, pp. 59–63, 2005.

[94] A. Oláh, H. Hillborg, and G. J. Vancso, “Hydrophobic recovery of UV/ozone treated poly(dimethylsiloxane): Adhesion studies by contact mechanics and mechanism of surface modification,” *Appl. Surf. Sci.*, vol. 239, no. 3–4, pp. 410–423, 2005.

[95] H. Hillborg and U. W. Gedde, “Hydrophobicity recovery of polydimethylsiloxane after exposure to corona discharges,” *Polymer (Guildf).*, vol. 39, no. 10, pp. 1991–1998, 1998.

[96] M. J. Kreder, J. Alvarenga, P. Kim, and J. Aizenberg, “Design of anti-icing surfaces: Smooth, textured or slippery?,” *Nat. Rev. Mater.*, vol. 1, no. 1, 2016.

[97] O. Parent and A. Ilinca, “Anti-icing and de-icing techniques for wind turbines: Critical review,” *Cold Reg. Sci. Technol.*, vol. 65, no. 1, pp. 88–96, 2011.

[98] S. Farhadi, M. Farzaneh, and S. A. Kulinich, “Anti-icing performance of superhydrophobic surfaces,” *Appl. Surf. Sci.*, vol. 257, no. 14, pp. 6264–6269, 2011.

[99] R. J. Bell, “Anti-icing properties of femtosecond laser surface processed material,” 2017.

[100] I. N. S. Based and I. W. Droplets, “Design of Ice-free Nanostructured Impacting Water Droplets,” *ACS Appl. Mater. Interfaces*, vol. 4, no. 12, pp. 7699−7707, 2010.

[101] E. B. Moore and V. Molinero, “Structural transformation in supercooled water controls the crystallization rate of ice,” *Nature*, vol. 479, no. 7374, pp. 506−508, 011.

[102] M.-H. Kim, D. R. Kim, and K.-S. Lee, “Stochastic approach to the anti-freezing

behaviors of superhydrophobic surfaces," *Int. J. Heat Mass Transf.*, vol. 106, pp.841−846, 2017.

[103] M. Schremb and C. Tropea, "Solidification of supercooled water in the vicinity of a solid wall," *Phys. Rev. E*, vol. 94, no. 5, p. 52804, Nov. 2016

[104] M. Nauenberg, "Conical tip in frozen water drops," *arXiv*, vol. 95064, p. 6, 2014.

[105] Q. Zhang, M. He, J. Chen, J. Wang, Y. Song, and L. Jiang, "Anti-icing surfaces based on enhanced self-propelled jumping of condensed water microdroplets," *Chem. Commun.*, vol. 49, no. 40, pp. 4516–4518, 2013.

[106] N. Wang, D. Xiong, Y. Deng, Y. Shi, and K. Wang, "Mechanically robust superhydrophobic steel surface with anti-icing, UV-durability, and corrosion resistance properties," *ACS Appl. Mater. Interfaces*, vol. 7, no. 11, pp. 6260–6272, 2015.

[107] S. A. Kulinich, S. Farhadi, K. Nose, and X. W. Du, "Superhydrophobic surfaces: Are they really ice-repellent?," *Langmuir*, vol. 27, no. 1, pp. 25–29, 2011.

[108] P. Guo, Y. Zheng, M. Wen, C. Song, Y. Lin, and L. Jiang, "Icephobic/anti-icing properties of micro/nanostructured surfaces," *Adv. Mater.*, vol. 24, no. 19, pp. 2642–2648, 2012.

[109] M. Ruan, W. Li, B. Wang, B. Deng, F. Ma, and Z. Yu, "Preparation and anti-icing behavior of superhydrophobic surfaces on aluminum alloy substrates," *Langmuir*, vol. 29, no. 27, pp. 8482–8491, 2013.

[110] Y. Wang, J. Xue, Q. Wang, Q. Chen, and J. Ding, "Verification of icephobic/anti-icing properties of a superhydrophobic surface," *ACS Appl. Mater. Interfaces*, vol. 5, no. 8, pp. 3370–3381, 2013.